Geophys. J. Int. (2003) **155,** 696–714

Comparison of azimuthal seismic anisotropy from surface waves and finite strain from global mantle-circulation models

Thorsten W. Becker,[1] James B. Kellogg,[2] Göran Ekström[2] and Richard J. O'Connell[2]

[1] *Cecil H. and Ida M. Green Institute of Geophysics and Planetary Physics, Scripps Institution of Oceanography, University of California, San Diego,* 9500 *Gilman Drive, La Jolla,* CA 92093, *USA. E-mail: tbecker@igpp.ucsd.edu*

[2] *Department of Earth and Planetary Sciences, Harvard University,* 20 *Oxford Street, Cambridge* MA 02138, *USA*

Accepted 2003 July 14. Received 2003 July 2; in original form 2003 January 9

SUMMARY

We present global models of strain accumulation in mantle flow to compare the predicted finite-strain ellipsoid (FSE) orientations with observed seismic anisotropy. The geographic focus is on oceanic and young continental regions where we expect our models to agree best with azimuthal anisotropy from surface waves. Finite-strain-derived models and alignment with the largest FSE axes lead to better model fits than the hypothesis of alignment of fast propagation orientation with absolute plate motions. Our modelling approach is simplified in that we are using a linear viscosity for flow and assume a simple relationship between strain and anisotropy. However, results are encouraging and suggest that similar models can be used to assess the validity of assumptions inherent in the modelling of mantle convection and lithospheric deformation. Our results substantiate the hypothesis that seismic anisotropy can be used as an indicator for mantle flow; circulation-derived models can contribute to the establishment of a quantitative functional relationship between the two.

Key words: finite strain, intraplate deformation, mantle convection, plate driving forces, seismic anisotropy.

1 INTRODUCTION

Seismic wave propagation in the uppermost mantle is anisotropic, as has been demonstrated using a variety of methods and data sets (e.g. Hess 1964; Forsyth 1975; Anderson & Dziewonski 1982; Vinnik *et al.* 1989; Montagner & Tanimoto 1991; Schulte-Pelkum *et al.* 2001). Vertically polarized waves propagate more slowly than horizontally polarized waves in the upper ∼220 km of the mantle, implying widespread transverse isotropy with a vertical symmetry axis. Surface wave studies have established lateral variations in the pattern of this radial anisotropy (e.g. Ekström & Dziewonski 1998). Inverting for azimuthal anisotropy (where the fast propagation axis lies within the horizontal) is more difficult, partly because of severe trade-offs between model parameters (e.g. Tanimoto & Anderson 1985; Laske & Masters 1998). Ongoing efforts to map azimuthal anisotropy in 3-D using surface waves (e.g. Montagner & Tanimoto 1991) are reviewed by Montagner & Guillot (2000).

The existence of anisotropy in upper-mantle rocks can be associated with accumulated strain due to mantle convection (e.g. McKenzie 1979), as reviewed by Montagner (1998). The use of seismic anisotropy as an indicator for mantle and lithospheric flow is therefore an important avenue to pursue since other constraints for deep mantle flow are scarce. There are currently few quantitative models that connect anisotropy observations to the 3-D geometry of mantle convection, and this paper describes our attempts to fill that gap using Rayleigh wave data and global circulation models.

Surface wave studies can place constraints on variations of anisotropy with depth, but the lateral data resolution is limited. Alternative data sets such as shear wave splitting measurements have the potential to image smaller-scale lateral variations, though they lack depth resolution (e.g. Silver 1996; Savage 1999). However, an initial comparison between observations and synthetic splitting from surface wave models showed poor agreement between results from both approaches (Montagner *et al.* 2000). A possible reason for this finding is that the modelling of shear wave splitting measurements needs to take variations of anisotropy with depth into account (e.g. Schulte-Pelkum & Blackman 2003). The predicted variations of finite strain with depth from geodynamic models can be quite large (e.g. Hall *et al.* 2000; Becker 2002), implying that a careful treatment of each set of *SKS* measurements might be required. We will thus focus on surface-wave-based observations of azimuthal anisotropy for this paper and try to establish a general understanding of strain accumulation in 3-D flow. In subsequent models, other observations of anisotropy should also be taken into account.

1.1 Causes of seismic anisotropy

Anisotropy in the deep lithosphere and upper mantle is most likely to be predominantly caused by the alignment of intrinsically anisotropic olivine crystals (lattice-preferred orientation, LPO) in mantle flow (e.g. Nicolas & Christensen 1987; Mainprice *et al.*

2000). Seismic anisotropy can therefore be interpreted as a measure of flow or velocity gradients in the mantle and has thus received great attention as a possible indicator for mantle convection (e.g. McKenzie 1979; Ribe 1989; Chastel *et al.* 1993; Russo & Silver 1994; Buttles & Olson 1998; Tommasi 1998; Hall *et al.* 2000; Blackman & Kendall 2002). There is observational (Ben Ismail & Mainprice 1998; Little *et al.* 2002) and theoretical evidence (Wenk *et al.* 1991; Ribe 1992) that rock fabric and the fast shear wave polarization axis will line up with the orientation of maximum extensional strain. (We shall distinguish between *directions*, which refer to vectors with azimuths between 0° and 360°, and *orientations*, which refer to two-headed vectors with azimuths that are 180° periodic. We will also use the term *fabric* loosely for the alignment of mineral assemblages in mantle rocks such that there is a pronounced spatial clustering of particular crystallographic axes around a specific orientation, or in a well-defined plane.) More specifically, we expect that for a general strain state, the fast (a), intermediate (c), and slow (b) axes of olivine aggregates will align, to first order, with the longest, intermediate and shortest axes of the finite-strain ellipsoid (Ribe 1992). The degree to which the fast axes cluster around the largest principal axis of the finite strain ellipsoid (FSE), or, alternatively, the orientation of the shear plane, will vary and may depend on the exact strain history, temperature, mineral assemblage of the rock and possibly other factors (e.g. Savage 1999; Tommasi *et al.* 2000; Blackman *et al.* 2002; Kaminski & Ribe 2002). The simple correlation between FSE and fabric may therefore not be universally valid. For large-strain experiments, the fast propagation orientations were found to rotate into the shear plane of the experiment (Zhang & Karato 1995), an effect that was caused partly by dynamic recrystallization of grains and that is accounted for in some of the newer theoretical models for fabric formation (e.g. Wenk & Tomé 1999; Kaminski & Ribe 2001, 2002). Further complications for LPO alignment could be induced by the presence of water (Jung & Karato 2001).

Instead of trying to account for all of the proposed anisotropy formation mechanisms at once, we approach the problem by using global flow models to predict the orientation of finite strain in the mantle. We then compare the anisotropy produced by these strains to the seismic data, using a simplified version of Ribe's (1992) model. We focus on oceanic plates where the lithosphere should be less affected by inherited deformation (not included in our model) than in continental areas. The agreement between predicted maximum extensional strain and the fast axes of anisotropy is found to be good in most regions, which supports the inferred relationship between strain and fabric in the mantle. We envision that future, improved global circulation models can be used as an independent argument for the validity and the appropriate parameter range of fabric development models such as that of Kaminski & Ribe (2001), and intend to expand on our basic model in a next step.

2 AZIMUTHAL ANISOTROPY FROM RAYLEIGH WAVES

Tomographic models with 3-D variations of anisotropy based on surface waves exist (e.g. Montagner & Tanimoto 1991; Montagner 2002). However, since there are some concerns about the resolving power of such models (e.g. Laske & Masters 1998), we prefer to compare our geodynamic models directly with a few azimuthally anisotropic phase-velocity maps from inversions by Ekström (2001). In this way, we can avoid the complications that are involved in a 3-D inversion.

Phase velocity perturbations, δc, for weak anisotropy can be expressed as a series of isotropic, D^0, and azimuthally anisotropic terms with π-periodicity, $D^{2\phi}$, and $\pi/2$-periodicity, $D^{4\phi}$ (Smith & Dahlen 1973):

$$\delta c = \frac{dc}{c} \approx D^0 + D_C^{2\phi}\cos(2\phi) + D_S^{2\phi}\sin(2\phi) + D_C^{4\phi}\cos(4\phi) + D_S^{4\phi}\sin(4\phi), \quad (1)$$

where ϕ denotes azimuth. $D^{2\phi}$ and $D^{4\phi}$ anisotropy imply that there are one and two fast propagation orientations in the horizontal plane, respectively. As discussed in the Appendix, fundamental-mode Rayleigh waves are typically more sensitive to anisotropy variations with 2ϕ dependence than Love waves; we will thus focus on Rayleigh waves.

The kernels for surface wave sensitivity to 2ϕ anisotropy have a depth dependence for Rayleigh waves that is similar to their sensitivity to variations in v_{SV} (Montagner & Nataf 1986) with maximum sensitivity at ∼70, ∼ 120, ∼ 200 km depth for periods of 50, 100 and 150 s, respectively (see the Appendix). Fig. 1 shows phase-velocity maps from inversions by Ekström (2001) for those periods. Ekström used a large data set (∼120 000 measurements) and a surface-spline parametrization (1442 nodes, corresponding to ∼5° spacing at the equator) to invert for lateral variations in the D terms of eq. (1). To counter the trade-off between isotropic and anisotropic structure, Ekström (2001) damped 2ϕ and 4ϕ terms 10 times more than the isotropic D^0 parameters. The inversion method will be discussed in more detail in a forthcoming publication, and the resolving power for $D^{2\phi}$ anisotropy will be addressed in Section 5.1. Here, we shall only briefly discuss some of the features of the anisotropy maps.

The isotropic and 2ϕ anisotropic shallow structure imaged in Fig. 1 appears to be dominated by plate-tectonic features such as the well-known seafloor spreading-pattern, where D^0 increases with plate age and $D^{2\phi}$ is oriented roughly parallel to the spreading direction close to ridges (e.g. Forsyth 1975; Montagner & Tanimoto 1991). There are, however, deviations from this simple signal, and the $D^{2\phi}$ pattern in the Western Pacific and southwestern parts of the Nazca Plate has no obvious relation to current plate motions. The patterns in anomaly amplitudes are quantified in Fig. 2. We show the correlation of D^0, $D^{2\phi}$ and $D^{4\phi}$ variations with tectonic regionalizations and plate-motion amplitudes. The isotropic signal shows a positive correlation with sea-floor age for $T = 50$ s, since ridges are where slow wave speeds are found; this signal is lost for deeper sensing phases. In particular, for $T = 50$ s, both convergent and divergent plate boundaries are found to be seismically slow, which is reflected in a negative correlation coefficient, r, with the radial velocities from flow models, $|v_r|^{\text{avg}}$. D^0 is also positively correlated with cratons for all periods, because the continental tectosphere is generally imaged as fast structure by tomography.

There is a negative correlation of D^0 with horizontal velocities; this is partly the consequence of positive r with continental regions because oceanic plates move faster than continental ones. The $D^{2\phi}$ signal has a negative correlation with cratons for all T, and a positive correlation with horizontal and radial velocities for $T \geq 100$ s. The observed weaker regional anisotropy underneath cratons might be due to the higher viscosity of continental keels (and hence less rapid shearing) and/or frozen in fabric with rapidly varying orientations, which is averaged out by the surface wave inversion. Positive r for $D^{2\phi}$ with plate speeds in turn may be caused by more rapid shearing underneath oceanic plates. However, this last conclusion in particular is weakened by the uneven raypath coverage which limits tomographic inversions. The ability of Ekström's (2001) data set to recover synthetic $D^{2\phi}$ structure is reflected by the correlation of the $D^{2\phi}$-recovery function, $D_r^{2\phi}$, from Section 5.1, shown as open

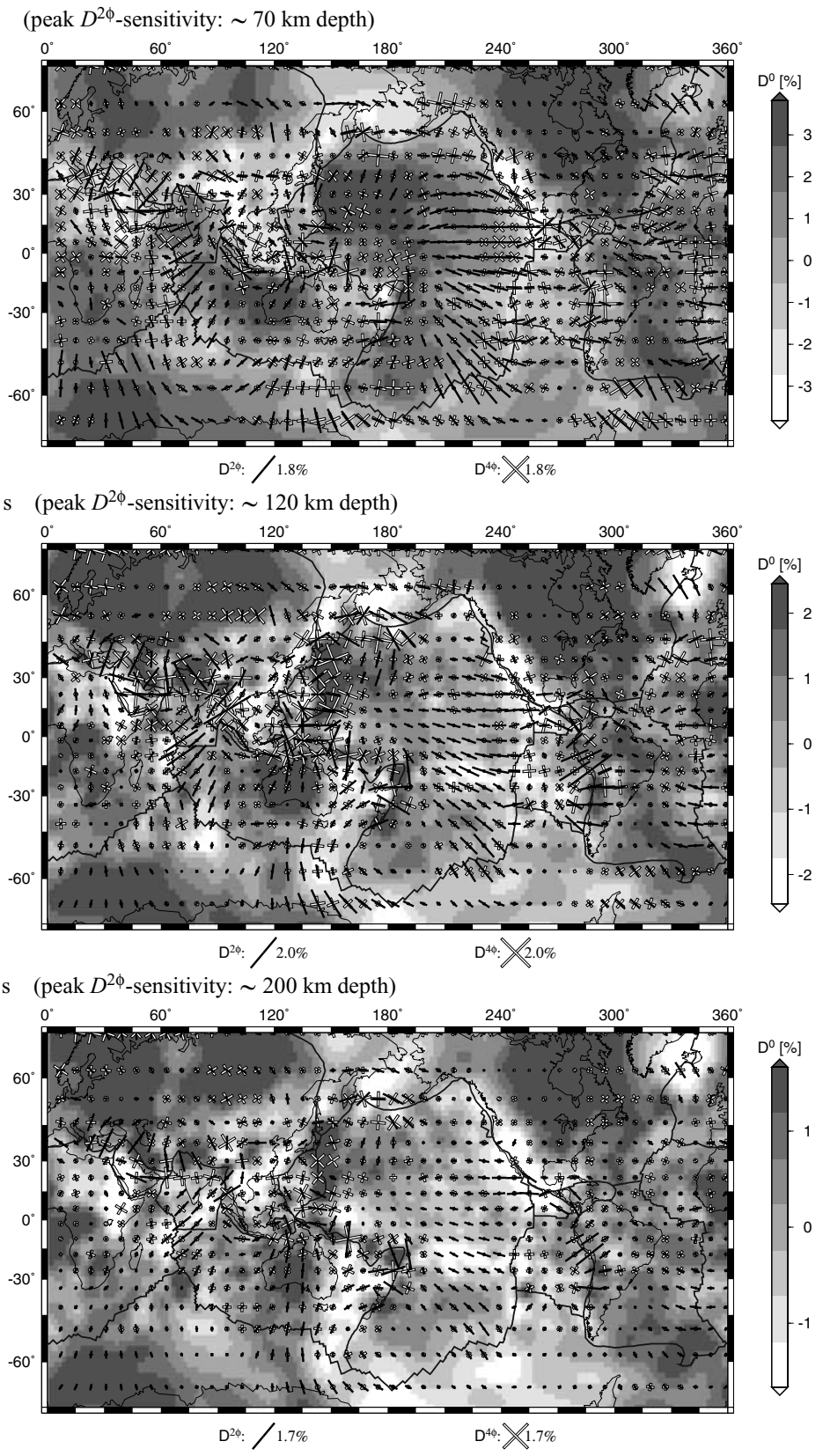

Figure 1. Isotropic and anisotropic variations of phase velocity for Rayleigh waves at periods, T, of (a) 50 s, (b) 100 s and (c) 150 s from Ekström (2001). We show isotropic anomalies as background shading (D^0 term in eq. (1), colourbars clipped at 50 per cent of maximum anomaly), $D^{2\phi}$ fast orientations as sticks, and $D^{4\phi}$ terms as crosses with maximum amplitude as indicated in the legend. $D^{2\phi}$ sensitivity peaks at ∼70, ∼ 120 and ∼200 km depth for 50, 100 and 150 s, respectively (see the Appendix).

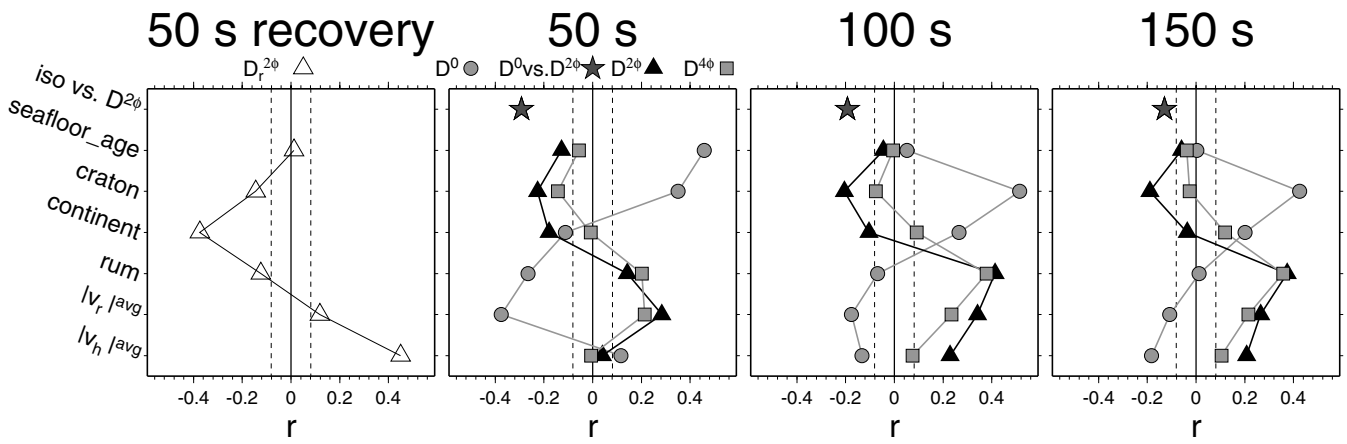

Figure 2. Correlation coefficient, r, for $T = 50$ s recovery test and surface wave models of Fig. 1 at periods of 50, 100 and 150 s. We show isotropic anomaly (D^0, circles), 2ϕ anisotropy ($D^{2\phi}$ amplitude, filled triangles) and 4ϕ anisotropy ($D^{4\phi}$ amplitude, squares) correlations with seafloor-age, cratons and continental regionalizations (from Nataf & Ricard 1996), uppermost mantle slabs (rum, average upper 400 km from Gudmundsson & Sambridge 1998), average absolute radial ($|v_r|^{\rm avg}$) and horizontal ($|v_h|^{\rm avg}$) velocities from a flow calculation based on plate motions (upper 400 km average, no-net-rotation frame) and *smean_nt* (Section 3.1). Stars indicate r between the isotropic and $D^{2\phi}$ signal, and open triangles for the leftmost plot the correlations of surface wave inversion $D^{2\phi}$ amplitude-recovery, $D_r^{2\phi} = \log_{10}(D^{2\phi}_{\rm recovered}/D^{2\phi}_{\rm model})$, as discussed in Section 5.1. All fields are expanded up to spherical harmonic degree $\ell_{\rm max} = 31$ before calculating r; vertical dashed lines indicate the corresponding 99 per cent significance level assuming bi-normal distributions.

triangles in Fig. 2. As a consequence of the event–receiver geometry, recovery of azimuthal anisotropy is better in the oceanic plates than in the continents, which leads to a positive and negative r of $D_r^{2\phi}$ with horizontal plate speeds and the continental function, respectively.

If anisotropy were purely due to a clearly defined fast propagation axis in the horizontal plane, we would expect the $D^{4\phi}$ signal to be much smaller than $D^{2\phi}$ for fundamental-mode Rayleigh waves (see Montagner & Nataf 1986, and the Appendix). The 4ϕ signal in Fig. 1 is indeed smaller than that from 2ϕ, but it is not negligible. Both 4ϕ and 2ϕ amplitudes are positively correlated with plate boundaries ($|v_r|^{\rm avg}$ in Fig. 2), especially with convergent margins where slabs are found (*rum* in Fig. 2). This might indicate that the predominantly vertical orientation of strain in these regions (Section 3.4) causes the symmetry axis of anisotropy to have a large radial component. However, we will proceed to interpret only the $D^{2\phi}$ signal for simplicity and compare the observed fast axes with the horizontal projection of the longest axis of the flow-derived FSEs. Some of the largest deviations between our models and observations are in the regions of large $D^{4\phi}$ (Section 5.2). This could be caused by either poor resolution of the data or a breakdown of our model assumptions concerning anisotropy, or both.

3 MODELLING STRAIN AND LPO ANISOTROPY

We predict seismic anisotropy by calculating the finite strain that a rock would accumulate during its advection through mantle flow (e.g. McKenzie 1979). Given a velocity field that is known as a function of time and space, the passive-tracer method lends itself to the problem of determining strain as outlined below.

3.1 Modelling flow

We use the method of Hager & O'Connell (1981) to model circulation in the mantle. The Stokes equation for incompressible flow in the infinite Prandtl number regime,

$$\nabla \cdot \boldsymbol{\tau} = \nabla p - \rho \mathbf{g}, \tag{2}$$

with $\boldsymbol{\tau}$, p, ρ and $\mathbf{g}$ denoting deviatoric stress, pressure, density and gravitational acceleration, respectively, is solved for a constitutive equation where the viscosity, η, varies only radially. A spherical harmonic expansion of all physical quantities is used, plate velocities are prescribed as surface boundary conditions, the core–mantle boundary is free-slip, and internal density variations are scaled from seismic tomography. We can then solve (2) for the instantaneous velocities in a realistic 3-D geometry. One of the major limitations of this approach is that η is not allowed to vary laterally. However, we think that the method is accurate enough to give us a good first-order estimate of large-scale flow in the mantle.

Our choice of input models (Table 1) and viscosity structures (Fig. 3) is motivated by previous studies (e.g. Hager & Clayton 1989; Ricard & Vigny 1989; Mitrovica & Forte 1997; Lithgow-Bertelloni & Silver 1998; Steinberger 2000) and our own work on comparing mantle models (Becker & Boschi 2002) and inverting for plate velocities (Becker & O'Connell 2001a). Mantle density structure is taken either directly from slab models, or from tomography where

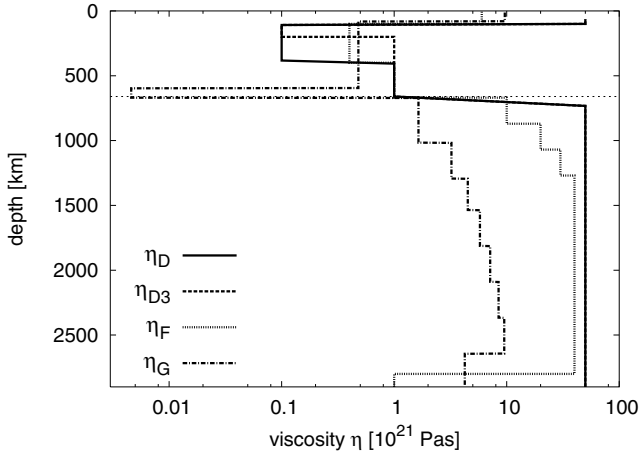

Figure 3. Mantle viscosity profiles as used for the flow modelling: $\eta_{\rm D}$ (weak asthenosphere, from Hager & Clayton 1989), $\eta_{\rm D3}$ (thinner asthenospheric channel), $\eta_{\rm F}$ (Steinberger 2000) and $\eta_{\rm G}$ (Mitrovica & Forte 1997). The dotted horizontal line indicates 660 km depth.

Table 1. Mantle density models used for the flow calculations (see Becker & Boschi 2002, for details), z indicates depth. We use the tectonic regionalizations from 3SMAC by Nataf & Ricard (1996).

Name	Type	$R^S{}_\rho$ density scaling for tomography	Source
lrr98d	Slab model, slablets sink at parametrized speeds	—	Lithgow-Bertelloni & Richards (1998)
stb00d	Slab model, includes advection in 3-D flow	—	Steinberger (2000)
ngrand	*S*-wave tomography	0.2 for $z > 220$ km 0.0 for $z \leq 220$ km	S. Grand's web site as of June 2001
ngrand_nt	*ngrand* with anomalies in cratonic regions from 3SMAC removed	0.2	*ngrand*
smean	Mean *S*-wave model based on published models	0.2 for $z > 220$ km 0.0 for $z \leq 220$ km	Becker & Boschi (2002)
smean_nt	*smean* with anomalies in cratonic regions from 3SMAC removed	0.2	*smean*

we scale velocity anomalies to density using a constant factor

$$R_\rho^S = d \ln \rho / d \ln v \tag{3}$$

of 0.2 for *S*-wave models for all depths below 220 km, and zero elsewhere to account for the tectosphere where velocity anomalies may image compositional heterogeneity. For density models *ngrand_nt* and *smean_nt*, we also include shallow structure above 220 km but only away from cratons by masking out the regions given by 3SMAC (Nataf & Ricard 1996).

For all purely plate-motion-related flow, the predicted circulation is focused in the upper-mantle since viscosity increases in the lower mantle. The shallow asthenospheric channel in η_D and η_F (Fig. 3) results in a pronounced maximum in radial flow at ∼300 km depth, while the low-viscosity 'notch' at 660 km that characterizes η_G leads to an abrupt change between upper- and lower-mantle horizontal velocities. The rate of decrease of horizontal velocities with depth in the upper mantle is smaller for η_G than for η_F because there is less drag exerted by the lower mantle. Since this implies slower shallow straining for the η_G models, we will consider η_G as an end-member case alongside the more generic η_F. However, the physical mechanisms that might lead to an η_G-type viscosity profile are only poorly understood (e.g. Panasyuk & Hager 1998), and we consider η_F to be closer to the current consensus on the average viscosity of the mantle.

Plate-motion-related flow can provide a good approximation for large-scale, near-surface straining patterns. Such flow will, however, not be representative of the overall straining and mixing properties of the mantle, and we expect vigorous thermal convection to exhibit stronger currents at depth (e.g. van Keken & Zhong 1999). Hence, we also compare the flow characteristics of circulation models that include density in the mantle from tomography with a thermal convection model by Bunge & Grand (2000). Using their equation of state for consistency, we convert the present-day temperature field of Bunge & Grand's (2000) 3-D spherical calculation to density anomalies, and then recompute the corresponding instantaneous velocities using our method. Both the shape and amplitude of the variation of velocity amplitudes with depth are similar to what we obtain with our flow models using *ngrand*. Since Bunge & Grand's (2000) model is partly constructed such that the temperature heterogeneity matches that inferred from tomography, we should indeed expect that the profiles look similar. However, the similarity indicates that our scaled density anomalies are of the right order and dynamically consistent (Becker & O'Connell 2001a).

Our flow calculation uses Newtonian rheology, as would be expected for the diffusion-creep regime of the high-temperature deep mantle (e.g. Ranalli 1995). However, lattice-preferred orientation of olivine, and hence LPO-related anisotropy, forms only under dislocation creep, which is characterized by a stress weakening power law. We expect that Newtonian mantle flow will be similar to power-law creep regionally, and therefore think that velocities in our models should resemble the actual large-scale circulation patterns in the mantle. However, deviations between flow for linear and non-linear creep could be substantial at smaller scales, and a quantitative study of 3-D circulation with power-law rheology to validate our assumptions remains to be undertaken.

3.1.1 No net rotation

All of our flow calculations are performed in the no-net-rotation (NNR) reference frame since our model cannot generate any net rotation of the lithosphere as it has no lateral viscosity contrasts (O'Connell *et al.* 1991; Ricard *et al.* 1991). A prescribed net rotation of the surface would not produce any strain, but simply lead to a rotation of the whole mantle. Fast anisotropy orientations are, however, often compared with absolute plate motions in a hotspot reference frame (APM, e.g. Vinnik *et al.* 1992). In the simplest hypothesis, the orientation of velocity vectors in the APM frame at the surface is supposed to be indicative of a simple shear layer in an asthenospheric channel, causing straining between the plates and a stationary deep mantle.

Since lateral viscosity variations exist in the mantle, a net rotation may be generated by convection. However, as shown by Steinberger & O'Connell (1998), the net rotation component in hotspot reference frames may be biased owing to the relative motion of hotspots. We will compare our NNR-frame-derived strains with the quasi-null hypothesis of a correlation between anisotropy and surface-velocity orientations below. A better fit is obtained for strain-derived anisotropy, leading us to question the hypothesis of alignment with surface velocities alone, both for the APM and NNR reference frames.

3.1.2 Reconstructing past mantle circulation

We show in Section 4.2 that strain accumulation at most depths is sufficiently fast that, under the assumption of ongoing reworking of fabric, the last tens of Myr are likely to dominate present-day strain and anisotropy. However, we include results where our velocity fields are not steady state but change with time according to plate-motion reconstructions and backward-advected density fields. We use reconstructions from Gordon & Jurdy (1986) and Lithgow-Bertelloni *et al.* (1993) within the original time periods without interpolating between plate configurations during any given stage.

To avoid discontinuities in the velocity field, the transition at the end of each tectonic period is smoothed over ≈1 per cent of the respective stage length; velocities change to that of the next stage according to a $\cos^2$-tapered interpolation. The width of this smoothing interval was found to have little effect on the predicted long-term strain accumulation.

While we can infer the current density anomalies in the mantle from seismic tomography, estimates of the past distributions of buoyancy sources are more uncertain. To model circulation patterns for past convection, we also advect density anomalies backward in time using the field method of Steinberger (2000). We neglect diffusion, heat production and phase changes, and assume adiabatic conditions. These simplifications make the problem more tractable, but advection can be numerically unstable under certain conditions (e.g. Press *et al.* 1993, p. 834ff). To damp some short-wavelength structure which is artificially introduced into the density spectrum at shallow depths, we taper the density time derivative using a $\cos^2$ filter for $\ell \geq 0.75\ell^{\rho}_{\max}$. With this approximate method, we obtain satisfactory results for backward advection when compared with a passive tracer method in terms of overall structure. However, tracers are, as expected, better at preserving sharp contrasts, because the field method suffers from numerical diffusion.

While active tracer methods (e.g. Schott *et al.* 2000) and backward convection models (e.g. Conrad & Gurnis 2003) would be better suited for problems in which the detailed distribution of density anomalies matters, we shall not be concerned with any improvement of the backward advection scheme at this point. The results from inversions that pursue a formal search for optimal mantle-flow histories such that the current density field emerges (Bunge *et al.* 2003) should eventually be used for strain modelling. However, in so far as fabric does not influence the pattern of convection significantly, the method we present next is completely general; it can also be applied to a velocity field that has been generated with more sophisticated methods than we employ here.

3.2 The tracer method

We use a fourth-order Runge–Kutta scheme with adaptive stepsize control (e.g. Press *et al.* 1993, p. 710) to integrate numerically the tracer paths through the flow field. All fractional errors are required to be smaller than 10^{-7} for all unknowns, including the finite strain matrix as outlined below. For this procedure, we need to determine the velocity at arbitrary locations within the mantle. Velocities and their first spatial derivatives are thus interpolated with cubic polynomials (e.g. Fornberg 1996, p. 168) from a grid expansion of the global flow fields. Mantle velocities are expanded on $1^\circ \times 1^\circ$ grids with typical radial spacing of ∼100 km; they are based on flow calculations with maximum spherical harmonic degree $\ell_{\max} = 63$ for plate motions and $\ell_{\max} = 31$ for density fields (tomographic models are typically limited to long wavelengths, *cf.* Becker & Boschi 2002). To suppress ringing introduced by truncation at finite ℓ, we use a $\cos^2$ taper for the plate motions. We conducted several tests of our tracer advection scheme, and found that we could accurately follow closed streamlines for several overturns.

3.3 Finite strain

The strain accumulation from an initial $\mathbf{x}$ to a final position $\mathbf{r}$ can be estimated by following an initial infinitesimal displacement vector $d\mathbf{x}$ to its final state $d\mathbf{r}$ (e.g. Dahlen & Tromp 1998, p. 26ff). We define the deformation-rate tensor $\boldsymbol{G}$ based on the velocity $\mathbf{v}$ as

$$\boldsymbol{G} = (\boldsymbol{\nabla}_{\mathbf{r}}\mathbf{v})^{\mathrm{T}}. \tag{4}$$

Here, $\boldsymbol{\nabla}_{\mathbf{r}}$ is the gradient with respect to $\mathbf{r}$ and T indicates the transpose. For finite strains, we are interested in the deformation tensor $\boldsymbol{F}$,

$$\boldsymbol{F} = (\boldsymbol{\nabla}_{\mathbf{x}}\mathbf{r})^{\mathrm{T}}, \tag{5}$$

where $\boldsymbol{\nabla}_{\mathbf{x}}$ is the gradient with respect to the tracer $\mathbf{x}$, because $\boldsymbol{F}$ transforms $d\mathbf{x}$ into $d\mathbf{r}$ as

$$d\mathbf{r} = \boldsymbol{F} \cdot d\mathbf{x} \quad \text{or} \quad d\mathbf{x} = \boldsymbol{F}^{-1} \cdot d\mathbf{r}. \tag{6}$$

The latter form with the inverse of $\boldsymbol{F}$, $\boldsymbol{F}^{-1}$, (which exists for realistic flow) allows us to solve for the deformation that corresponds to the reverse path from $\mathbf{r}$ to $\mathbf{x}$. To obtain $\boldsymbol{F}$ numerically, we make use of the relation between $\boldsymbol{G}$ and $\boldsymbol{F}$:

$$\frac{\partial}{\partial t}\boldsymbol{F} = \boldsymbol{G} \cdot \boldsymbol{F}, \tag{7}$$

where $\partial/\partial t$ denotes the time derivative. Our algorithm calculates $\boldsymbol{G}$ at each time step to integrate eq. (7) (starting from $\boldsymbol{F} \equiv \mathbf{I}$ at $\mathbf{x}$, where $\mathbf{I}$ denotes the identity matrix) with the same Runge–Kutta algorithm that is used to integrate the tracer position from $\mathbf{x}$ to $\mathbf{r}$. To ensure that volume is conserved, we set the trace of $\boldsymbol{G}$ to zero by subtracting any small non-zero divergence of $\mathbf{v}$ that might result from having to interpolate $\mathbf{v}$. We tested our procedure of estimating $\boldsymbol{F}$ against analytical solutions for simple and pure shear (McKenzie & Jackson 1983).

The deformation matrix can be polar-decomposed into an orthogonal rotation $\mathbf{Q}$ and a symmetric stretching matrix in the rotated reference frame, the left-stretch matrix $\mathbf{L}$, as

$$\boldsymbol{F} = \mathbf{L} \cdot \mathbf{Q} \quad \text{with} \quad \mathbf{L} = (\boldsymbol{F} \cdot \boldsymbol{F}^{\mathrm{T}})^{1/2}. \tag{8}$$

For the comparison with seismic anisotropy, we are only interested in $\mathbf{L}$, which transforms an unstrained sphere at $\mathbf{r}$ into an ellipsoid that characterizes the deformation that material accumulated on its path from $\mathbf{x}$ to $\mathbf{r}$. The eigenvalues of $\mathbf{L}$,

$$\lambda_1 > \lambda_2 > \lambda_3, \tag{9}$$

measure the length and the eigenvectors the orientation of the axes of that finite strain ellipsoid at $\mathbf{r}$ after the material has undergone rotations.

Our approach is similar to that of McKenzie (1979), as applied to subduction models by Hall *et al.* (2000). However, those workers solve eq. (7) by central differences while we use Runge–Kutta integration. Moreover, Hall *et al.*, calculate the FSE based on $\mathbf{B}^{-1}$, where

$$\mathbf{B}^{-1} = \left(\boldsymbol{F}^{-1}\right)^{\mathrm{T}} \cdot \boldsymbol{F}^{-1}. \tag{10}$$

Hall *et al.*, define a stretching ratio, s_i, from the deformed to the undeformed state in the direction of the ith eigenvector of $\mathbf{B}^{-1}$ with eigenvalue γ_i as $s_i = 1/\sqrt{\gamma_i}$. Since $\mathbf{B}$ is equivalent to $\mathbf{L}^2$, and $\mathbf{B}$ as well as $\mathbf{L}$ are symmetric, both approaches yield the same results when we identify the λ_i with the s_i after sorting accordingly. Numerically, $\mathbf{L}^2$ is faster to calculate since it does not involve finding the inverse of $\boldsymbol{F}$.

3.3.1 Anisotropy based on the FSE

We introduce *natural strains* as a convenient measure of stretching

$$\zeta = \ln\left(\frac{\lambda_1}{\lambda_2}\right) \quad \text{and} \quad \xi = \ln\left(\frac{\lambda_2}{\lambda_3}\right), \tag{11}$$

following Ribe (1992) who shows that the orientations of fast shear wave propagation rapidly align with maximum stretching eigenvectors in numerical deformation experiments, regardless of the initial conditions. After ζ and $\xi \gtrsim 0.3$, there are essentially no further fluctuations in fast orientations. Using a logarithmic measure of strain is also appropriate based on the other result of Ribe (1992) that the amplitude of seismic anisotropy grows rapidly with small linear strain and levels off at larger values, above $\zeta \sim 0.7$. When we average fast strain orientations with depth for the comparison with seismic anisotropy, we weight by ζ to incorporate these findings. This is a simplification since some of Ribe's (1992) experiments indicate a more rapid saturation of anisotropy amplitude at large strains. However, differences between logarithmic and linear averaging of strain orientations are usually not large. We therefore defer a more detailed treatment of the anisotropy amplitudes to future work when we can incorporate fabric development more realistically, e.g. using Kaminski & Ribe's (2001) approach.

We formulate the following *ad hoc* rules to determine the finite strain from circulation models.

(1) Follow a tracer that starts at its present-day location **r** backward in time for a constant time interval, τ, to an initially unknown origin location **x** while keeping track of the deformation $\boldsymbol{F}'$ ($\tau \sim$ 5 Myr). Then, calculate the strain that would have accumulated if the tracer were to move from an unstrained state at **x** to **r**, given by $(\boldsymbol{F}')^{-1}$. Such an approach would be appropriate if fabric formation were only time-dependent; the $\tau \rightarrow 0$ result is related to the instantaneous strain rates.

(2) Alternatively, define a threshold strain ζ_c above which any initial fabric gets erased, as would be expected from the results of Ribe (1992) ($\zeta_c \sim 0.5$). In this case, we only have to advect backward until ζ or ξ, as based on $(\boldsymbol{F}')^{-1}$, reaches ζ_c; we match $\zeta(\mathbf{r})$ to ζ_c within 2 per cent. The tracer trajectory will correspond to different time intervals depending on the initial position of the tracer (Section 4.2).

We stop backward advection in both schemes if tracers originate below 410 km depth, where we expect that the phase transition of olivine (e.g. Agee 1998) will erase all previous fabric. For most of the models, we will consider the flow field as a steady state but not advect back in time for more than 43 Myr, the age of the bend in the Hawaii–Emperor seamount chain that marks a major reorganization of plate motions (e.g. Gordon & Jurdy 1986). Changes in plate motions affect only the very shallowest strains for continuous strain accumulation (Section 4.2).

3.4 Examples of finite strain accumulation

We examine strain accumulation by following individual tracers close to plate boundaries in order to develop an understanding of the global, convection-related strain field. Our examples are similar, and should be compared with, previous work (e.g. McKenzie 1979; Ribe 1989; Hall *et al.* 2000) but they are unique in that they are fully 3-D and based on estimates of mantle circulation that include realistic plate geometries.

For simplicity, the flow field used for our divergent margin example for the East Pacific Rise (EPR, Fig. 4) includes only plate-motion-related flow, calculated by prescribing NUVEL1 (DeMets *et al.* 1990) NNR velocities at the surface using viscosity profile η_F. The largest stretching axes align roughly perpendicular to the ridge and mostly in the horizontal plane. The ridge-related strain pattern has been observed globally for surface waves (e.g. Forsyth 1975; Nishimura & Forsyth 1989; Montagner & Tanimoto 1991) and *SKS* splitting (Wolfe & Solomon 1998) and can be readily interpreted in terms of a general plate tectonic framework (e.g. Montagner 1994).

For the strain evolution example at convergent margins (Fig. 5), we include *ngrand_nt* density in the flow calculation. Our FSE illustrations would be appropriate for a weak slab end-member case but will have limited applicability if lateral viscosity contrasts are significant (*cf.* Hall *et al.* 2000). The strain development can be divided into two stages: first, we see compression in the plane of the slab as material enters the mantle. The largest stretching axes are nearly radial, and the horizontal part of the FSE shows trench-parallel elongation. In the second stage, for greater depths and particularly owing to the inclusion of slab pull forces, deep stretching becomes more important and leads to deformations such that the largest stretching axes rotate mostly perpendicular to the trench and become more horizontal (Fig. 5c).

Where the largest eigenvector points in a nearly radial direction, the elongated horizontal part of the FSE approximately follows the trench geometry and shows varying degrees of trench-parallel alignment. In regions where measurements for *SKS* waves, travelling nearly radially, yield zero or small anisotropy but where more horizontally propagating local *S* phases show splitting (Fouch & Fischer 1998), this small horizontal deformation component may be important. This is particularly the case if crystallographic fast axes are distributed in a ring rather than tightly clustered around the largest FSE eigendirection, in which case the resolved anisotropy may be trench parallel. However, Hall *et al.* (2000) show that synthetic splitting is mostly trench-perpendicular in the backarc region for simple flow geometries, if fast wave propagation is assumed to be always oriented with the largest FSE axis. Escape flow around a slab that impedes large-scale currents in the mantle is therefore usually invoked as an explanation for trench-parallel splitting (e.g. Russo & Silver 1994; Buttles & Olson 1998). Yet, at least for some regions, 3-D circulation that is not due to slab impediment might be invoked alternatively (Hall *et al.* 2000; Becker 2002).

4 GLOBAL FINITE-STRAIN MAPS

4.1 Plate-scale circulation

Fig. 6(a) shows the global, $\tau = 10$ Myr time interval, depth-averaged strain field for a circulation calculation that incorporates only plate-related flow using η_F. For simplicity, plate motions are assumed to be constant in time for 43 Myr. We focus on the horizontal projection of the largest stretching direction of **L**, showing the orientation of the FSE axis as sticks for which the lengths scale with ζ. The background shading in Fig. 6 shows $\Delta L_{rr} = L_{rr} - 1$ as an indication of stretching in the radial, r, direction. Strain was calculated for $\sim$10 000 approximately evenly distributed tracers ($\approx 2^\circ$ spacing at the equator) for each layer, which were placed from 50–400 km depth at 50 km intervals to sample the upper mantle above the 410 km phase transition. The horizontal projections of the largest axes of the FSE are depth averaged after weighting them with the ζ-scaled strain at each location (Section 3.3), while the radial, ΔL_{rr}, part is obtained from a simple depth average. The horizontal strain orientations will be interpreted as a measure of the depth-averaged azimuthal anisotropy as imaged by Rayleigh waves.

The finite-strain field of Fig. 6(a) is similar to instantaneous strain rates in terms of the orientations of largest extension, which are dominated by the shearing of the upper mantle owing to plate motions. However, orientations are not identical to those expected to be

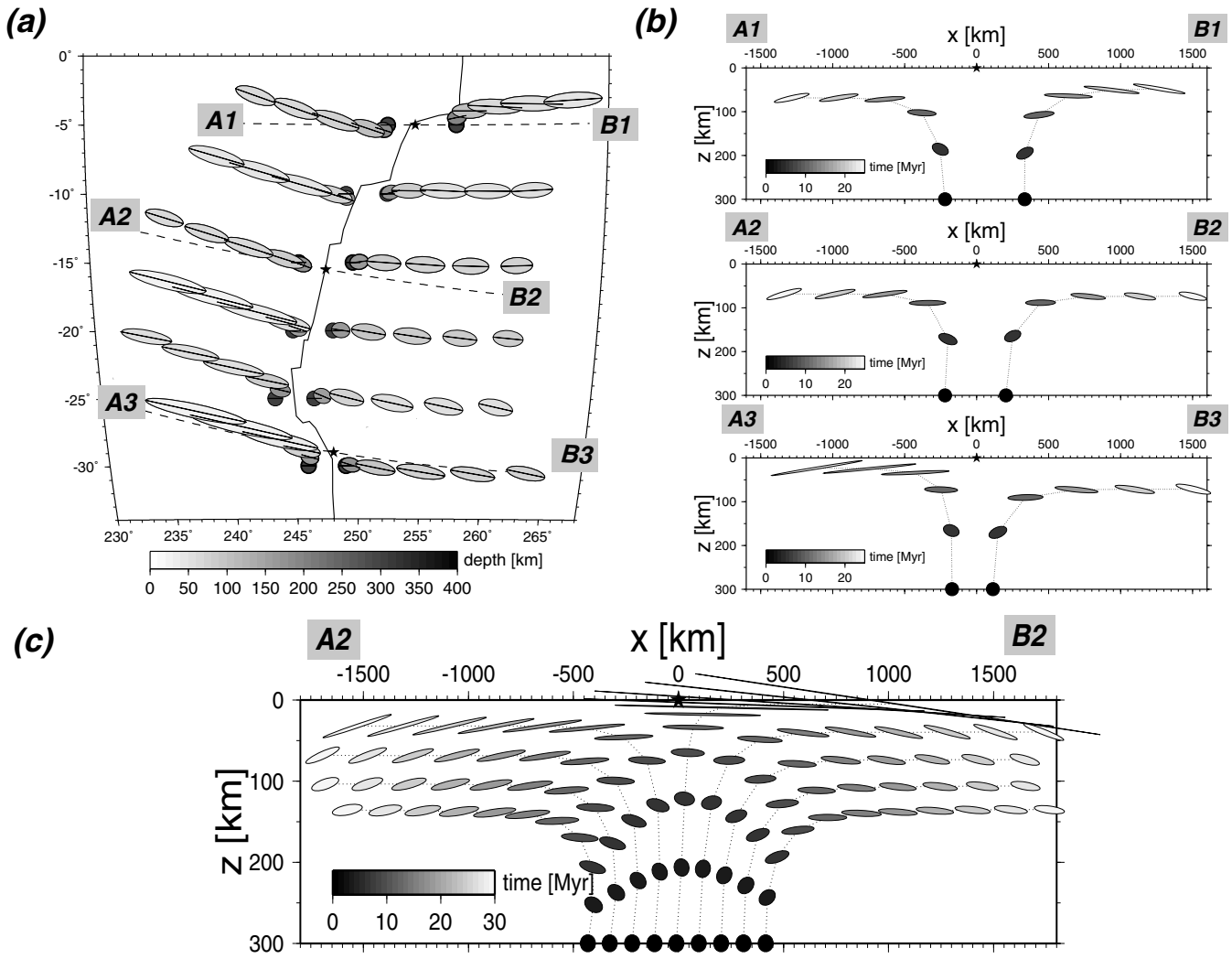

Figure 4. (a) Projection of the largest principal axes of strain ellipsoids (sticks) and a horizontal cut through FSEs (ellipses), shown centred at tracer positions in purely plate-motion-driven flow (η_F) around the East Pacific Rise. Tracer positions are shown at 5 Myr intervals, starting at 300 km depth, with depth greyscale-coded. (b) Projection of FSEs for profiles 1, 2 and 3 as indicated by dashed lines in (a), ellipse shading corresponds to time. (c) Time evolution of strain for an expanded set of tracers along profile 2 (surface projection not shown in (a)) with 2.5 Myr time intervals.

produced directly from the surface velocities because of 3-D flow effects. The depth-averaged strain for $\tau = 10$ Myr is furthermore dominated by radial extension (positive ΔL_{rr}) at both ridges and trenches, unlike for instantaneous strain (or small τ), where ridges are under average radial compression. This effect is due to the radial stretching of material that rises underneath the ridges before being pulled apart sideways and radially compressed at the surface. This effect has been invoked in qualitative models of radial anisotropy (e.g. Karato 1998) and may explain the fast v_{SV} ($v_{SV} > v_{SH}$ at $\sim$200 km depths) anomaly in surface wave models for the EPR (Boschi & Ekström 2002). Not surprisingly, strain accumulation for constant-τ models is strongest underneath the fast-moving oceanic plates.

Fig. 6(b) shows results for constant strain, $\zeta_c = 0.5$, assuming that this is a relevant 'reworking' strain after which all previous fabric is erased (Ribe 1992). Consequently, most horizontal strains are of comparable strength, with some exceptions, such as the Antarctic Plate around 30°W/60°S. There, shearing is sufficiently slow that it would take more than our cut-off time of 43 Ma to accumulate the ζ_c strain.

4.2 Mantle-density-driven flow

Fig. 7 shows $\zeta_c = 0.5$ depth-averaged strain for flow that includes the effect of plate-related motion plus internal densities as derived from tomography model *smean* (Table 1). With the caveat that we are interpreting the instantaneous flow that should be characteristic of mantle convection at the present day as a steady state for several tens of Myr, we find that the inclusion of mantle density leads to a concentration of radial flow and deformation underneath South America and parts of East Asia. These features are related to subduction where the circum-Pacific downwellings exert strong forces on the overlying plates (*cf.* Becker & O'Connell 2001b; Steinberger *et al.* 2001).

For η_F (Fig. 7a), smaller-scale structure owing to density anomalies is most clearly visible within continental plates, which were characterized by large-scale trends for plate motions alone. Other patterns include a west–east extensional orientation in East Africa, related to an upwelling that correlates with the rift-zone tectonics.

The predicted strain for η_G (Fig. 7b) is, expectedly, more complex. Since the low-viscosity notch of η_G partly decouples the upper and

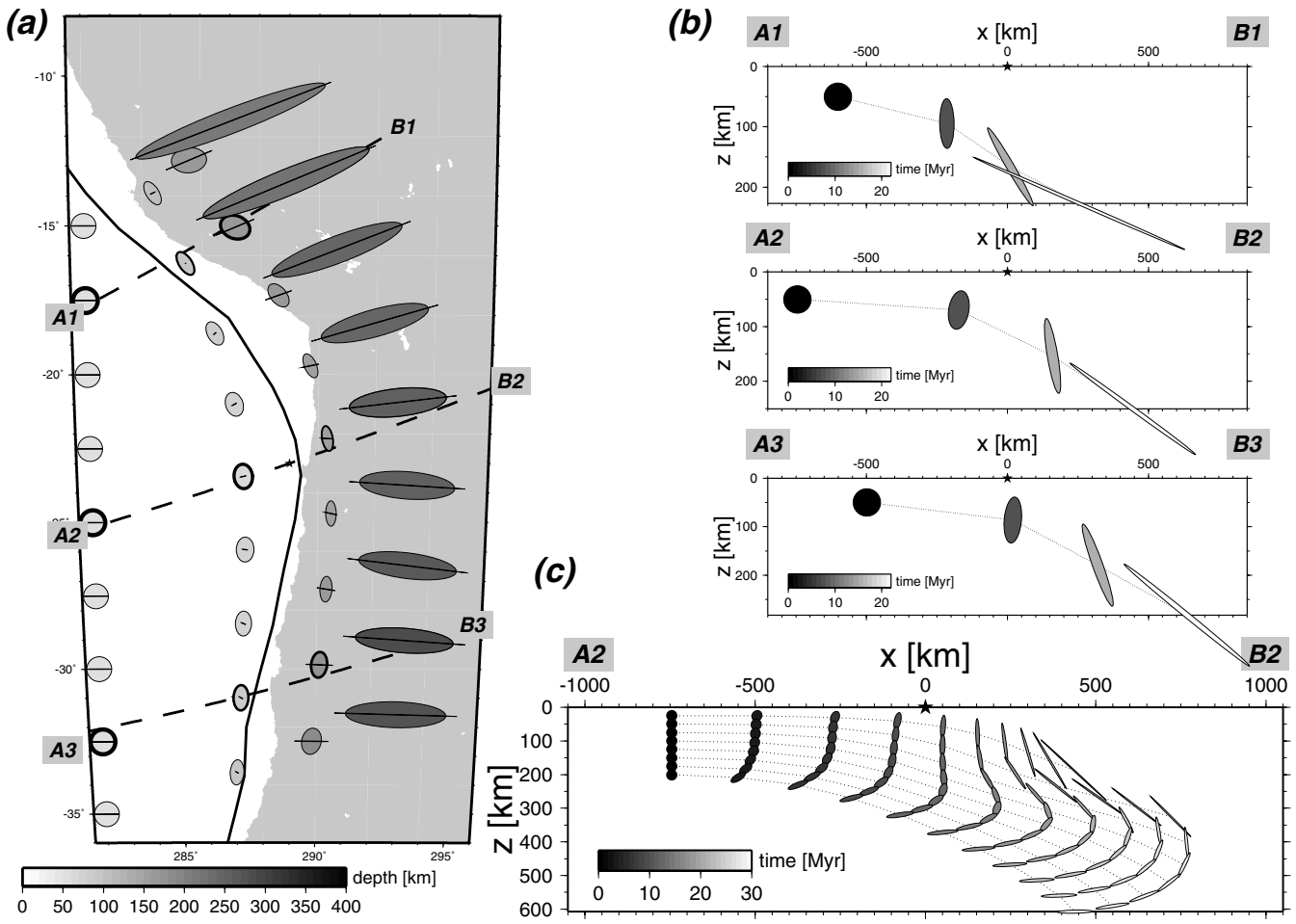

Figure 5. (a) Tracer paths in a *smean_nt* density-included flow field (η_F) at 5 Myr intervals for part of the South American subduction zone. Ellipses are drawn at tracer positions as in Fig. 4, moving from west to east and starting at 50 km depth in the Nazca plate. Note the variations in predicted slab dip along strike as indicated by the final depth of the tracer locations. (b) Projection of FSEs on profiles 1, 2 and 3 as shown in (a). (c) Finite strain accumulation along different streamlines close to profile 2 (surface trace not shown in (a)) with 2.5 Myr intervals.

lower mantle in terms of shearing, upwellings such as the one in the southwestern Pacific (the superswell region) are able to cause a stronger anisotropy signal than for the η_F model.

In contrast to the plate-motion-only models, finite strain from density-driven flow is quite sensitive to the input models and viscosity structures in terms of the local orientations of the largest stretching axes. This is to be expected, given that tracer advection will amplify small differences between tomographic models. Fig. 7 is therefore only an illustration of the large-scale features predicted by the lowest-common-denominator tomography model *smean*; individual high-resolution models (e.g. *ngrand*) lead to more irregular strain predictions, but not to better model fits (Section 5.2).

Fig. 8 shows histograms of age, the time required to achieve $\zeta_c = 0.5$ strain, for different depths based on the model shown in Fig. 7(a). We find that many of the shallow strain markers (within the high-viscosity lithospheric layer) have our age limit of $t_c = 43$ Ma, implying that strain accumulation is slow within the 'plates' that move coherently without large interior velocity gradients. For deeper layers, where shearing is stronger, strain is accumulated more rapidly such that $\zeta = 0.5$ is reached by most tracers before 20 Myr and at smaller horizontal advection distances than at shallow depth. Most regions of slow strain accumulation are underneath continents where minima in the amplitudes of surface velocities are found. In general, however, $\zeta \sim 0.5$ strains are accumulated in a few Myr and over small advection distances (∼500 km) for all but the shallowest depths.

The depth average of Fig. 7 hides some of the variations of the orientation of the largest strain with depth (Fig. 9). The cumulative rotation of the horizontal projection of the largest FSE axis between 400 km depth and the surface can be in excess of 180° (Becker 2002). Such complexity in strain is strong in, but not limited to, regions of predominantly radial flow (Figs 5 and 9). This finding may complicate the interpretation of anisotropy measurements, especially for body wave observations (Saltzer *et al.* 2000; Schulte-Pelkum & Blackman 2003). However, comparisons of our global horizontal projections of the largest principal axes of the FSE with observed splitting orientations indicate agreement between strain and splitting in (sparsely sampled) oceanic and in young continental regions, e.g. the western US (Becker 2002). In older continental regions (e.g. the eastern US and eastern South America) and shear-dominated regions (e.g. New Zealand and NE Tibet) agreement is poor. It is difficult to interpret these findings given the uneven distribution of the *SKS* data that samples mostly continents where we expect that our method will lead to less reliable estimates of anisotropy. To unravel the depth dependence of flow and strain, it seems most promising to focus future studies on regional observations

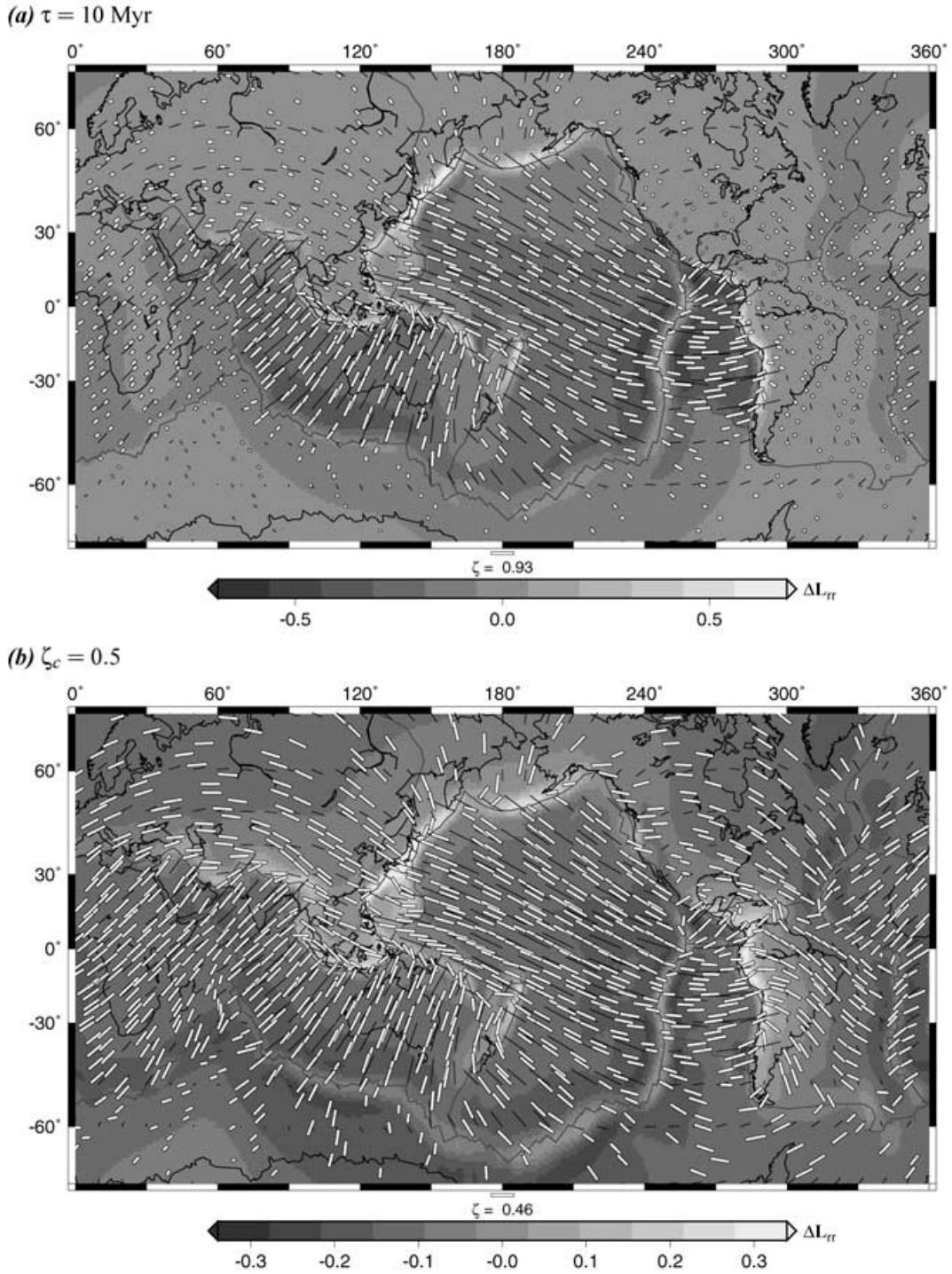

Figure 6. Depth-averaged (upper mantle, $50 \leq z \leq 400$ km) finite strain for $\tau = 10$ Myr (a) and $\zeta_c = 0.5$ (b) strain accumulation. We use plate-motion-related flow only and viscosity profile η_F. Thick sticks are plotted centred at every $\sim$ fifth tracer location and indicate the orientation of the horizontal projection of the largest axis of the FSE, scaled with the logarithmic strain, ζ. (See legend for ζ amplitudes, and note that strains in (a) are $\sim 2\times$ larger than in (b) underneath fast moving plates.) Background shading denotes $\Delta L_{rr} = L_{rr} - 1$, and thin sticks denote the orientation of surface plate motions from NUVEL1-NNR. Colourscale for ΔL_{rr} is clipped at 70 per cent of the maximum absolute value.

of anisotropy (e.g. Polet & Kanamori 2002; Simons & van der Hilst 2003).

4.3 Changes in plate motions

The global models described in the previous section were all based on steady-state flow with a cut-off age, t_c, of 43 Ma. We conducted additional experiments where we allowed for evolving plate boundaries and backward-advected density anomalies as described in Section 3.1.2. Given our finding of rapid shearing for large depths from above, results for $z \gtrsim 150$ km were, as expected, similar to the steady-state models; depth averages with uniform weight for each layer as in Fig. 7(a) are, thus, not strongly modified. Fig. 10 explores some of the variations in predicted strains for shallow depth, at

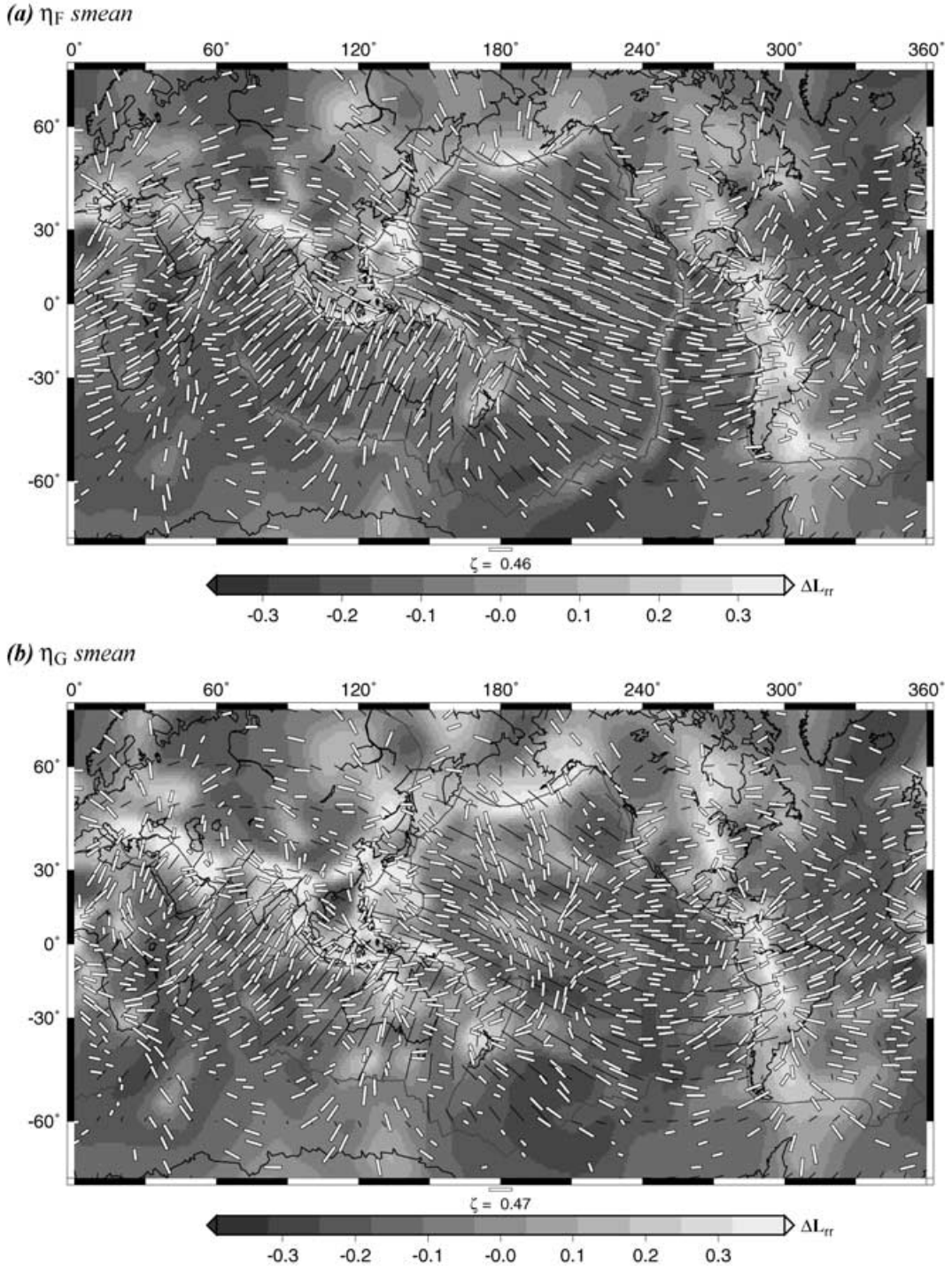

Figure 7. Depth-averaged finite strain for $\zeta_c = 0.5$ strain accumulation in plate-motion and *smean*-driven flow for viscosity profiles η_F (a, *cf.* Fig. 6b) and η_G (b). Thin sticks in the background are NNR plate velocities as in Fig. 6.

$z = 100$ km. Plate boundaries that change with time will introduce more complexity at small scales. We find that the large-scale effects of evolving plates are modest, however, even when we go back beyond the bend in the Hawaii–Emperor seamount chain. The shallow strain pattern underneath regions that move coherently for steady plate motions (Fig. 10a) is weakened or disrupted (Fig. 10b) since the smaller-scale density-related currents change over time. If we include non-tectosphere density from *smean* for $z < 220$ km, details in the fast orientations change slightly, and more pronounced straining occurs underneath Eastern Africa.

Since evolving plate boundaries mainly affect shallow structure, we can expect that *SKS*-based shear wave splitting observations will be only slightly modified by the uncertainties in such reconstructions and the overall effect of non-steady-state flow. For short-period surface waves with strong sensitivity to shallow structure, such as 50 s Rayleigh waves (see the Appendix), the effect may be larger.

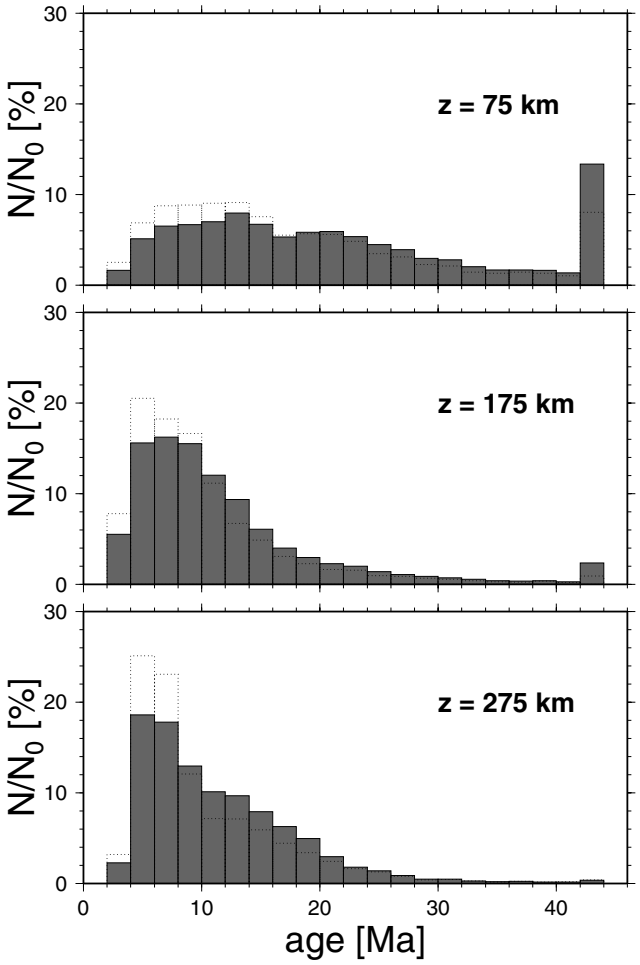

Figure 8. Histograms of tracer ages, i.e. duration for $\zeta_c = 0.5$ strain accumulation, for plate motion and *smean* related flow and η_F (Fig. 7a) for tracers that end up at 75, 175 and 275 km depth. N/N_0 denotes relative frequency, and tracer locations are chosen such that they evenly sample the surface. Dotted histograms are limited to tracers that end up in oceanic plate regions of 3SMAC (Nataf & Ricard 1996). Plate velocities are assumed to be steady state and the cut-off age is 43 Ma, hence the spike in the top panel corresponding to tracers that have not reached $\zeta = 0.5$ after 43 Ma. The age distributions correspond to a range of horizontal distances between initial and final tracer positions of up to ∼2000 km for 75 km depth, and the distribution maxima at ∼6 Ma for depths of 175 km and 275 km correspond to ∼250 km horizontal distance. Vertical distance travelled is ≲50 km.

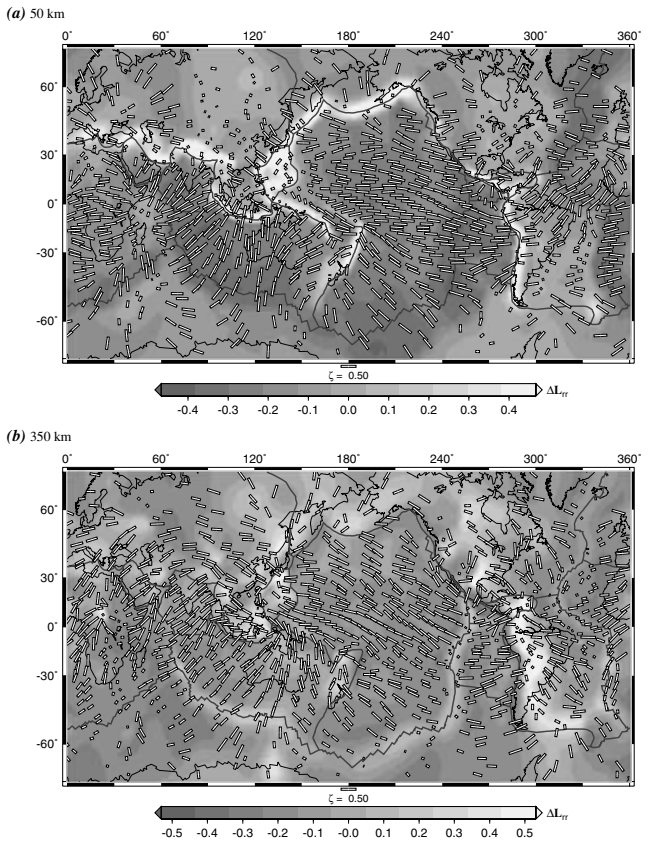

Figure 9. Largest FSE axes for a $\zeta_c = 0.5$ flow model including *smean* and profile η_F (Fig. 7a) shown at depths of (a) 50 km and (b) 350 km.

We therefore analyse whether strain predictions that include evolving plate boundaries lead to a better fit to the surface wave data than steady-state models (Section 5.2).

5 GLOBAL COMPARISON WITH SURFACE WAVES

5.1 Resolution of Rayleigh wave 2ϕ anisotropy inversions

Inversions of phase velocities for azimuthal anisotropy are complicated by trade-offs between isotropic and anisotropic structure (e.g. Laske & Masters 1998) and the uneven raypath coverage, which might map itself into apparent anisotropic structure (e.g. Tanimoto & Anderson 1985). To address these issues, we performed recovery tests, shown for Rayleigh waves at $T = 50$ s in Fig. 11. The same inversion procedure that was used to obtain the phase-velocity maps shown in Fig. 1 was employed to test our ability to recover a synthetic input model using the available data coverage. To make structure in the input model as realistic as possible, 2ϕ anisotropy was inferred from the steady-state circulation model using *smean*, η_F and $\zeta_c = 0.5$ (*cf.* Fig. 7a). The horizontal projections of the largest FSE axes were scaled with ζ to roughly account for the strength of inferred seismic anisotropy; we additionally weighted each layer according to the 50 s Rayleigh wave sensitivity kernel of Fig. A1. Maximum predicted strains were scaled to a 1.5 per cent 2ϕ anisotropy amplitude (resulting in 0.6 per cent rms variation) and the isotropic and $D^{4\phi}$ variations were set to zero. Random noise was added to mimic the observational uncertainties. The resulting variance reduction of the inversion was only 14 per cent for D^0, implying that little of the spurious signal was fitted. Fig. 11 shows that the orientations of azimuthal anisotropy of the input model are generally well recovered. Exceptions are found in the Middle East, in the Aleutians, the Cocos–Nazca plate area, and along the northern mid-Atlantic ridge system. To quantify these azimuthal deviations, we calculate the angular misfit $\Delta\alpha$ ($0^\circ \leq \Delta\alpha \leq 90^\circ$), shown in a histogram in Fig. 12(a). We also compute $\widehat{\Delta\alpha}$ by multiplying $\Delta\alpha$ by the input model amplitudes to give less weight to small-signal regions; $\widehat{\Delta\alpha}$ is shown as background shading in Fig. 11 and normalized such that weighted and original maximum deviations are identical.

The amplitude recovery of the test inversion is not as good as the azimuthal one. As shown in Fig. 2, recovery is worse on average in continental regions than in oceanic ones; there, regions of poor recovery are found in the southwest Indian Ocean, the northern Atlantic, the Scotia Plate region and the northwest Pacific. The average of the $\log_{10}$ of the recovered 2ϕ signal over the input 2ϕ amplitude,

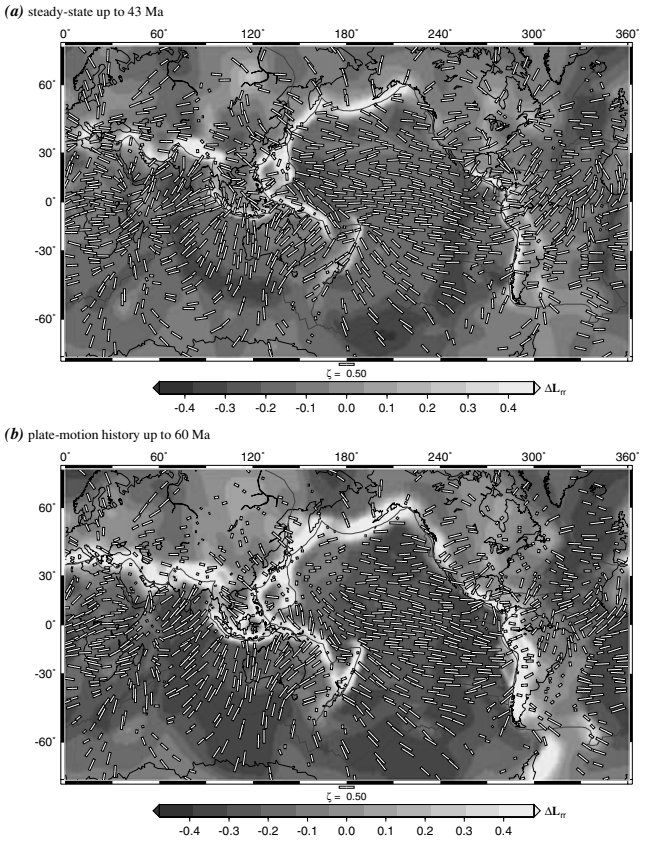

Figure 10. Largest FSE axes for $\zeta_c = 0.5$ at 100 km depth, η_F, and plate-motion and *smean* related flow. Plot (a) is from steady-state flow without evolving plates, allowing for tracer backtracking until the cut-off time $t_c =$ 43 Ma (Fig. 7a), (b) is for evolving plates and backward-advected *smean* densities until $t_c = 60$ Ma.

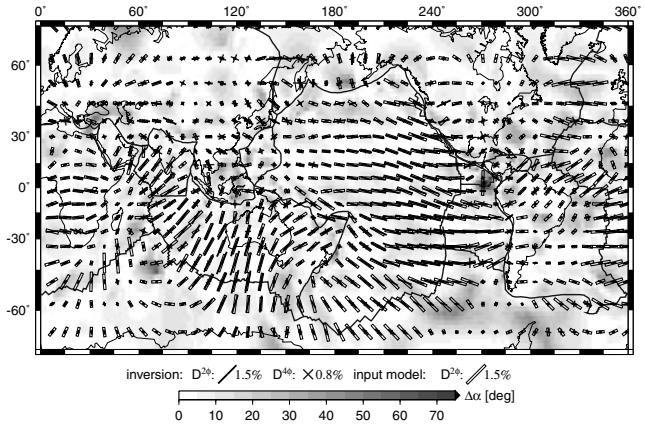

Figure 11. Input (open bars) and recovered (black sticks) azimuthal anisotropy for 50 s Rayleigh waves. The inverted structure has some artificial $D^{4\phi}$ anomalies (thin crosses), zero in the input model which is based on $\zeta_c = 0.5$, plate motions, and *smean* (*cf.* Fig. 7a). All anisotropy shown on the same, linear scale; maximum amplitudes are indicated below the map. Background shading is $\widehat{\Delta\alpha}$, the orientational deviation $\Delta\alpha$ scaled by the local $D^{2\phi}$ amplitude of the input model, normalized such that the maximum of $\widehat{\Delta\alpha}$ and $\Delta\alpha$ are identical.

$D_r^{2\phi}$, is -0.062, corresponding to a mean amplitude recovery of 86.7 per cent (Fig. 12b). Regions in which anisotropy strength is over-predicted are found at some trenches (e.g. Central Chile), where the inversion gives a trench-perpendicular signal, while the input

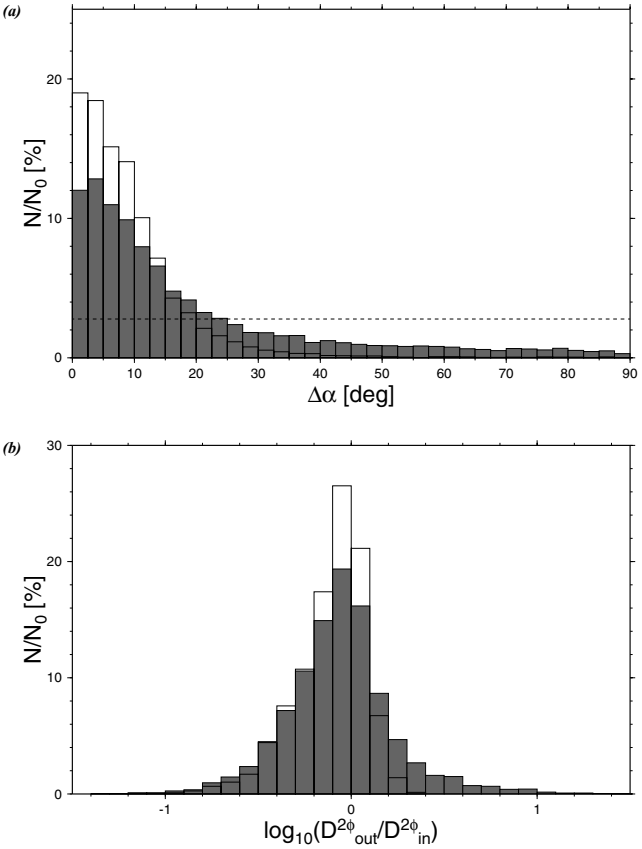

Figure 12. (a) Orientational misfit histogram $\Delta\alpha$ (grey bars) for equal-area spatial sampling of the recovery test of Fig. 11, N/N_0 denotes relative frequency. Open bars show misfit when restricted to regions with input $D^{2\phi}$ amplitudes $\geq$25 per cent of the maximum input. Dashed horizontal line denotes the expected random distribution of misfit. (b) Histogram of amplitude recovery, $D_r^{2\phi}$, as expressed by the decadic logarithm of inversion $D^{2\phi}$ over input $D^{2\phi}$ amplitudes (grey bars, open bars restricted to strong-amplitude input as in (a)).

model has small amplitude with FSEs being primarily radial. The area-weighted mean orientational misfit, $\langle\Delta\alpha\rangle$, is 18.8°, which is reduced to 13.4° if we weight the misfit by the input model 2ϕ amplitudes. Restricting ourselves further to oceanic lithosphere (as given by 3SMAC; Nataf & Ricard 1996), $\langle\Delta\alpha\rangle|_{oc} = 11.8°$. If we weight the global misfit by input and output model amplitudes (assuming small output amplitudes indicate poor resolution), $\langle\Delta\alpha\rangle =$ 9.9°. These values can guide us in judging misfits between observations and model predictions.

To evaluate the trade-offs that occur in the presence of coherent isotropic structure, we have analysed a second resolution test in which the random noise in the input D^0 signal was replaced by slowness anomalies derived from the crustal model CRUST5.1 (Mooney *et al.* 1998). The recovered anisotropic signal is similar to that of the first experiment, with mean azimuthal misfit $\langle\Delta\alpha\rangle =$ 13.7° (weighted by input $D^{2\phi}$) and mean amplitude recovery of 87.1 per cent for $D^{2\phi}$. If the 4ϕ terms are suppressed by damping them much more strongly than $D^{2\phi}$, the result is, again, similar to that shown in Fig. 11, but the azimuthal misfit and amplitude recovery are slightly improved to $\langle\Delta\alpha\rangle = 12.5°$ (weighted by input $D^{2\phi}$) and 90.3 per cent, respectively. Assuming that the $T = 50$ s results are representative of deeper-sensing waves, the resolution tests are encouraging since they imply that Ekström's (2001) inversions for azimuthal anisotropy are robust. The number of parameters of an

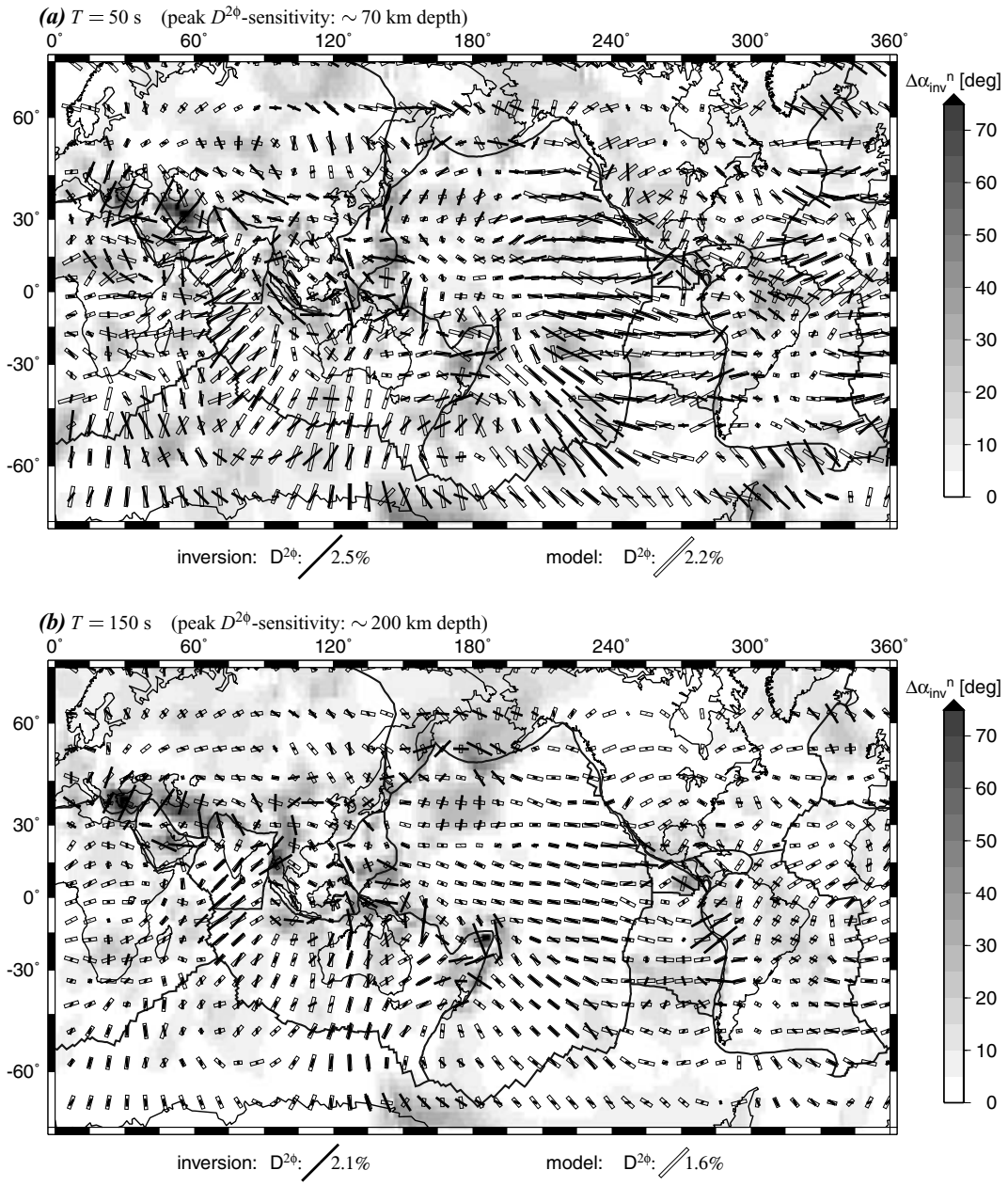

Figure 13. Comparison of Rayleigh wave 2ϕ-azimuthal anisotropy for $T = 50$ s (a) and $T = 150$ s (b), shown as black sticks (maximum $D^{2\phi}$ values shown to scale below map) and model anisotropy for $\zeta_c = 0.5$, evolving plates ($t_c = 60$ Ma), η_F, and *smean_nt* advected density, shown as open bars. We omit $D^{4\phi}$ from the inversions and scale the predicted anisotropy such that the rms $D^{2\phi}$ are identical to those from the inversions. To emphasize regions with large model misfit and strong surface wave signal, the background shading indicates azimuthal misfit scaled by the $D^{2\phi}$ amplitude of the phase velocity inversions such that the maximum scaled $\Delta\alpha$ is identical to the unweighted $\Delta\alpha$.

inversion for $D^{2\phi}$ is larger than that of an isotropic inversion and the corresponding increase in degrees of freedom cannot be justified based on the improvement in variance reduction alone (Laske & Masters 1998). However, the pattern that such an anisotropic inversion predicts is likely to be a real feature of the Earth and not an artefact.

5.2 Global azimuthal-anisotropy model fit

Fig. 13 compares maps for Rayleigh wave 2ϕ anisotropy from Ekström's (2001) inversions (Fig. 1) with predictions from our preferred geodynamic model, obtained by depth averaging (using the appropriate kernels) of the ζ-scaled horizontal projection of the largest axes of the FSE. The calculation uses $\zeta_c = 0.5$ strain and includes the effects of evolving plate motions, *smean_nt* buoyancy, and changes in plate configurations for $t_c = 60$ Ma. We find that much of the measured signal in the oceans can be explained by LPO orientations and finite strain as predicted from our global circulation model. We show a histogram of the angular misfit for $T = 50$ s in Fig. 14; the largest misfits are typically found in regions of small $D^{2\phi}$ amplitudes or in the continents, where anisotropy may be related to past deformation episodes.

The laterally averaged misfits are compared for several different models in Figs 15(a) and (b) for $T = 50$ and 150 s, respectively. We

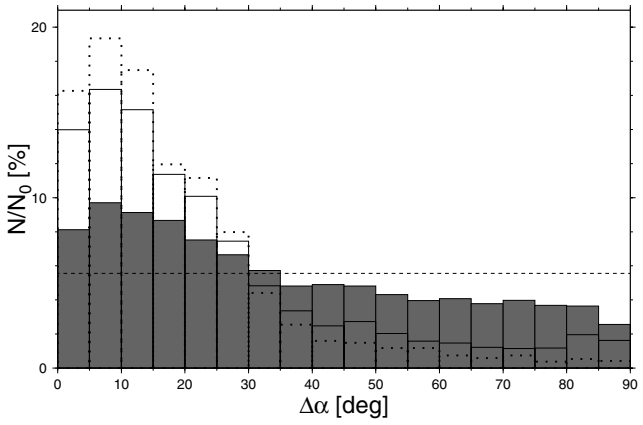

Figure 14. Histogram of orientational misfit, $\Delta\alpha$, between $T = 50$ s Rayleigh wave 2ϕ anisotropy and model prediction for $\zeta_c = 0.5$ strain, η_F, evolving plates ($t_c = 60$ Ma) and *smean_nt* advected density as in Fig. 13(a). Solid bars: all data; open bars: data restricted to regions where $D^{2\phi}$ of the inversion is $\geq$0.25 times its maximum; and open bars with dotted lines: further restricted to oceanic lithosphere. Dashed horizontal line indicates the expected random distribution of $\Delta\alpha$.

tried weighting the misfit in a number of ways but think that, in general, accounting for both the $D^{2\phi}$ amplitudes of the inversion and the model is most appropriate in order to avoid having poorly sampled regions bias $\langle\Delta\alpha\rangle$. For consistency, we have also weighted the surface plate-velocity-derived misfits (APM and NNR) by the model (i.e. plate-velocity) amplitudes. However, such velocity-weighted misfits are biased toward the oceanic plates, which move faster than continental ones, relative to $\zeta_c = 0.5$ strain models, which show a more uniform anisotropy amplitude globally (e.g. Fig. 7).

The selection of models in Fig. 15 allows the comparison of misfits for alignment with plate motions with misfits for FSE from purely plate-driven flow for different viscosities (labels: η_D, η_{D3}, 'base model' for η_F, and η_G, see Fig. 3). We find that most circulation-based strain models outperform the hypotheses of alignment with NNR or APM plate motions. This distinction in model quality supports our modelling approach and indicates that further study of finite strain models could lead to a better understanding of lithospheric deformation and mantle flow. The average fit to Ekström's (2001) anisotropy maps is better for shorter ($T = 50$ s in Fig. 15a) than for longer periods ($T = 150$ s in Fig. 15b). This could be due to differences in resolution of the surface waves, or the dominance of the plate-related strains at shallow depths, presumably the best-constrained large-scale features. We also observe a wider range in $\langle\Delta\alpha\rangle$ for different types of models at $T = 50$ s than at $T = 150$ s. This is expected, given that strains accumulate more rapidly at depth, so that it is, for instance, less important whether flow is treated as steady state or with evolving plate boundaries. For η_F, models that include buoyancy-driven flow lead to $\langle\Delta\alpha\rangle$ improvements of $\sim$6° compared with those with plate motions only. Comparing different density models, *smean* typically leads to better results than higher-resolution tomography (*ngrand*) or models that are based on slabs only (*stb00d* or *lrr98d*). Including shallow density variations underneath younger plate regions (non-tectosphere models, 'nt'), slightly improves the model fit.

Globally weighted results typically show the same dependence on model type as those that include only the oceanic lithosphere, $\langle\Delta\alpha\rangle|_{oc}$; the latter misfits are, however, generally smaller than the global estimates by $\sim$4°. The best models yield $\langle\Delta\alpha\rangle|_{oc} \approx 24°$ for $T = 50$ s and $\langle\Delta\alpha\rangle|_{oc} \approx 28°$ for $T = 100$ and 150 s, to be compared with 45° for random alignment, as well as $\approx$34° ($T = 50$ s) and $\approx$31° ($T = 100$ and 150 s) for alignment with plate velocities. Taking the resolution of the surface wave inversion as imaged by the $\widetilde{\Delta\alpha}$ function in Fig. 11 into account improves the misfit, but not significantly. Regional variations in misfit might therefore be due to poor surface wave resolution but, globally, $\Delta\alpha$ is independent of the surface wave resolution pattern.

There are a number of second-order observations that have guided us in the choice of the preferred model shown in Fig. 13. τ-limited (time-limited) strain-accumulation models lead to results that are similar to those of ζ models (strain-limited) without weighting. Results from τ calculations with $D^{2\phi}$ model-amplitude weighted $\langle\Delta\alpha\rangle$ are always, as expected, better than ζ models because of the additional bias that is introduced toward the oceans (where all models are more similar to the inversions). We therefore limit consideration to ζ_c models.

Fig. 15 also compares FSE misfits for *smean* density-included flow for different viscosity profiles (see the figure caption). We find better results for η_F than for η_G, with a $\sim$2° difference in $\langle\Delta\alpha\rangle$. (The large misfit of η_G models in the central Pacific as expected from Fig. 7 is partly offset by an improved fit in other regions such as the North-Western Pacific.) The more focused low-viscosity asthenospheric channel of η_{D3} (Fig. 3) also leads to a worse misfit than η_D or η_F, indicating a detrimental effect of a decoupling layer. Consistent with results for plate velocity inversions (Becker & O'Connell 2001a), we find that the simple Hager & Clayton (1989) profile η_D leads to equal or better misfit than η_F ($\langle\Delta\alpha\rangle$ better by $\sim$1°). We use η_F to explore different density models and flow estimates in Fig. 15 regardless, since η_F flow models are able to fulfil other geophysical constraints (e.g. Steinberger 2000).

For shallow ($T = 50$ s) structure where strain accumulation is representative of a longer timespan, $\langle\Delta\alpha\rangle$ values are slightly improved (not shown) when we include a 'freezing' mechanism for strains at shallow depths, where the temperature in the lithosphere might be too low for continuous fabric reworking (Becker 2002), but this is, again, partly due to the resulting bias toward the oceanic regions. We cannot find any significant global improvement compared with continuous strain-accumulation models. Comparing models with steady-state velocities or evolving plates in Fig. 15 we do, however, see a small ($\sim$2°) decrease in global misfit when the last 60 Myr of plate reconfiguration and density advection are taken into account.

In summary, we find that the strain produced by global mantle circulation is a valid explanation for the azimuthal anisotropy mapped by surface waves, and that such circulation-produced strain explains the pattern of azimuthal anisotropy better than does the pattern of absolute plate motions. Further exploration of regional and global model performance can guide us in our understanding of anisotropy in the upper mantle. While some of the regional misfit between model and anisotropy observations might be due to limitations in our method (such as the assumptions concerning the relationship between strain and imaged anisotropy, Section 2), others might indicate real effects such as intraplate deformation (e.g. in the Australian Plate), which we have not accounted for so far. Short-period surface waves with good shallow sensitivity may provide us with constraints on the strain history for times longer than a few tens of Myr and allow us to evaluate the degree of mantle–lithosphere coupling in different tectonic settings.

6 CONCLUSIONS

Observations of seismic anisotropy in the upper mantle can largely be explained by global circulation models under the assumption that

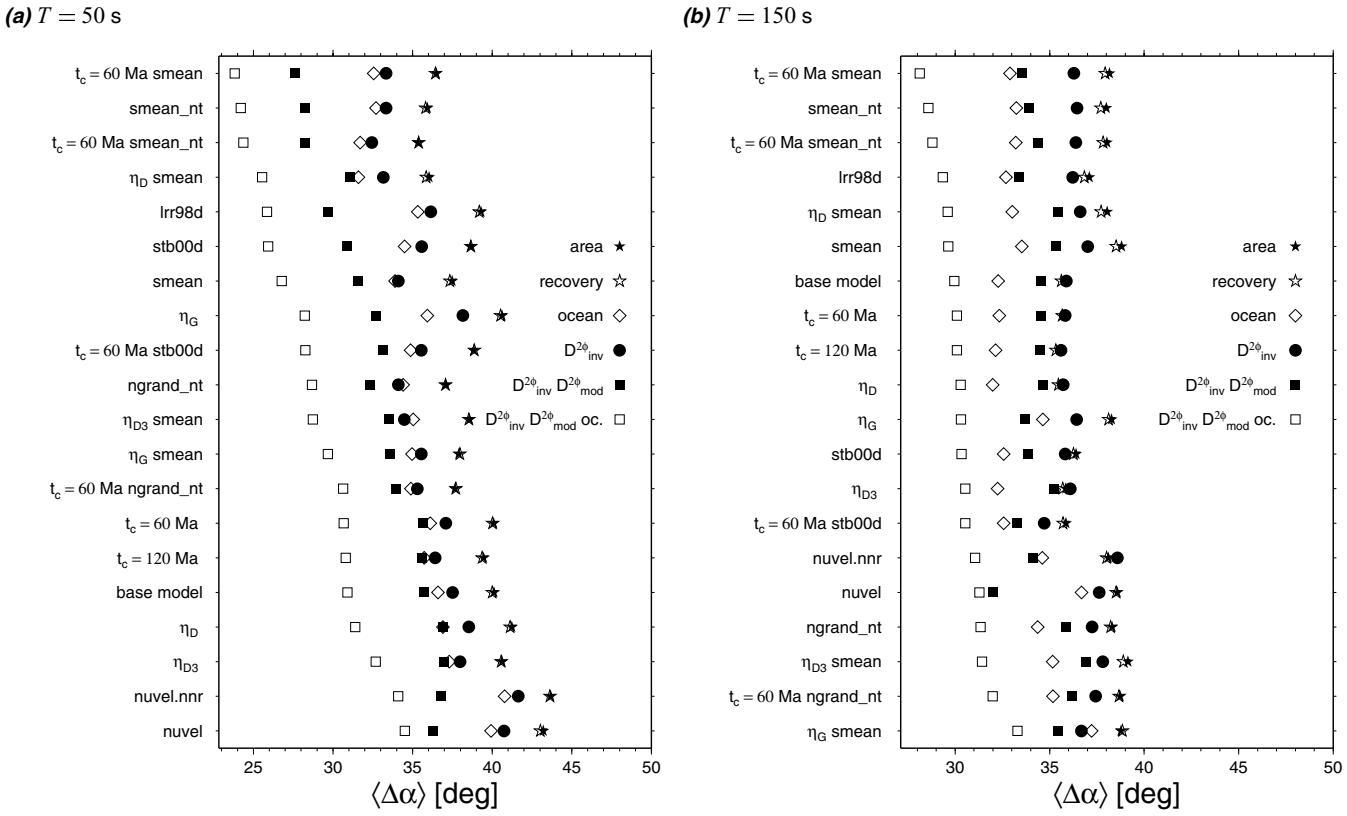

Figure 15. Mean orientational misfit between 2ϕ anisotropy of Rayleigh waves at $T = 50$ s (a, *cf.* Figs 13a and 14) and $T = 150$ s (b, *cf.* Fig. 13b) for a selection of surface plate velocities and circulation-derived, $\zeta_c = 0.5$ finite-strain models. The *y*-axis shows results for different models; all are based on plate-motion related flow and viscosity profile η_F unless indicated otherwise. We compare the azimuthal misfit for alignment with surface plate motions (labels: *nuvel* and *nuvel.nnr* for hotspot (HS2, APM) or NNR reference frames, respectively) with alignment with FSE from purely plate-driven flow for different viscosities (labels: η_D, η_{D3}, 'base model' for η_F, and η_G, see Fig. 3), and alignment with FSE from *smean* density-included flow (labels: 'η_D *smean*', 'η_{D3} *smean*', ' *smean*' for η_F, and 'η_G *smean*'). We also show results for different density models for η_F (see Table 1), and different flow models: If no time interval is specified, velocities are steady state with a cut-off in backward advection time, t_c, of 43 Ma; '$t_c = 60$ Ma' or '$t_c = 120$ Ma' denotes backward advection using evolving plate-boundaries and possibly density sources until t_c. The misfits, $\langle\Delta\alpha\rangle$, are obtained by area-weighted averaging over a grid interpolation of predicted and observed anisotropy (filled stars). We additionally weight models by the surface wave recovery function $\widetilde{\Delta\alpha}$ as shown in the background of Fig. 13 (open stars, mostly hidden by filled ones), restrict misfit to oceanic regions (open diamonds), weight by the inversion's $D^{2\phi}$ amplitude (filled circles), the inversion's and the model's $D^{2\phi}$ amplitudes (filled boxes), and the latter quantity furthermore restricted to oceanic plates (open boxes). (For APM and NNR velocities, weighting by the model amplitudes implies a strong bias toward the oceanic plates relative to $\zeta_c = 0.5$ models.) If we randomize the 2ϕ orientations of our models, we find a standard deviation of $\approx 0.4^\circ$ indicating that $\langle\Delta\alpha\rangle \lesssim 43^\circ$ is significantly different from the random mean of 45° at the 5σ level.

fast orientations are aligned with the largest axis of the finite strain ellipsoid, as suggested by the theory of Ribe (1992). Our models are very simplified in that we are using a linear viscosity for the flow calculations and assume that anisotropy obeys a straightforward relationship with finite strain. However, it is encouraging that mantle-flow-derived models lead to smaller misfits with azimuthal anisotropy inferred from surface waves than models based on alignment with surface velocities. A coupled model that uses the strain history predicted from a, possibly more sophisticated, circulation model as input for fabric development algorithms such as that of Kaminski & Ribe (2001) should be attempted next. In this way, we should be able to both evaluate the validity of our model assumptions and the generality of theories concerning the origin of seismic anisotropy and tectonic deformation in the upper mantle.

ACKNOWLEDGMENTS

We thank Neil Ribe for his constructive review. All figures were produced with the GMT software by Wessel & Smith (1991). Bernhard Steinberger provided the original version of the flow code used for the circulation calculation, which would not have been possible without numerous authors' willingness to share inversion and model results. Discussions with Karen Fischer and Paul Silver furthered our understanding of the implications of shear wave splitting measurements.

NOTE ADDED IN PROOF

After submission of this typescript, a similar study was published independently by Gaboret *et al.* (2003) with focus on the Pacific Plate.

REFERENCES

Agee, C.B., 1998. Phase transformations and seismic structure in the upper mantle and transition zone, in *Ultrahigh-Pressure Mineralogy. Physics and Chemistry of the Earth's Deep Interior, Reviews in Mineralogy,*

Vol. 37, pp. 165–203, ed. Hemley, R.J., Mineralogical Society of America, Washington DC.

Anderson, D.L. & Dziewonski, A.M., 1982. Upper mantle anisotropy: evidence from free oscillations, *Geophys. J. R. astr. Soc.,* **69,** 383–404.

Becker, T.W., 2002. Lithosphere–mantle interactions, *PhD thesis,* Harvard University, Cambridge.

Becker, T.W. & Boschi, L., 2002. A comparison of tomographic and geodynamic mantle models, *Geochem. Geophys. Geosyst.,* **3** (2001GC000168).

Becker, T.W. & O'Connell, R.J., 2001a. Predicting plate velocities with geodynamic models, *Geochem. Geophys. Geosyst.,* **2** (2001GC000171).

Becker, T.W. & O'Connell, R.J., 2001b. Lithospheric stresses caused by mantle convection: the role of plate rheology (abstract), *EOS, Trans. Am. geophys. Un.,* **82**(47), T12C–0921.

Ben Ismail, W. & Mainprice, D., 1998. An olivine fabric database; an overview of upper mantle fabrics and seismic anisotropy, *Tectonophysics,* **296,** 145–157.

Blackman, D.K. & Kendall, J.-M., 2002. Seismic anisotropy of the upper mantle: 2. Predictions for current plate boundary flow models, *Geochem. Geophys. Geosyst.,* **3** (2001GC000247).

Blackman, D.K., Wenk, H.-R. & Kendall, J.-M., 2002. Seismic anisotropy of the upper mantle: 1. Factors that affect mineral texture and effective elastic properties, *Geochem. Geophys. Geosyst.,* **3** (2001GC000248).

Boschi, L. & Ekström, G., 2002. New images of the Earth's upper mantle from measurements of surface-wave phase velocity anomalies, *J. geophys. Res.,* **107,** doi: 10.1029/2000 JB 000059.

Bunge, H.-P. & Grand, S.P., 2000. Mesozoic plate-motion history below the northeast Pacific Ocean from seismic images of the subducted Farallon slab, *Nature,* **405,** 337–340.

Bunge, H.-P., Hagelberg, C.R. & Travis, B.J., 2003. Mantle circulation models with variational data assimilation: inferring past mantle flow and structure from plate motion histories and seismic tomography, *Geophys. J. Int.,* **152,** 280–301.

Buttles, J. & Olson, P., 1998. A laboratory model of subduction zone anisotropy, *Earth planet. Sci. Lett.,* **164,** 245–262.

Chastel, Y.B., Dawson, P.R., Wenk, H.-R. & Bennett, K., 1993. Anisotropic convection with implications for the upper mantle, *J. geophys. Res.,* **98,** 17 757–17 771.

Conrad, C.P. & Gurnis, M., 2003. Seismic tomography, surface uplift, and the breakup of Gondwanaland: Integrating mantle convection backwards in time, *Geochem. Geophys. Geosyst.,* **4** (2001GC000299).

Dahlen, F.A. & Tromp, J., 1998. *Theoretical Global Seismology,* Princeton University Press, Princeton.

DeMets, C., Gordon, R.G., Argus, D.F. & Stein, S., 1990. Current plate motions, *Geophys. J. Int.,* **101,** 425–478.

Ekström, G., 2001. Mapping azimuthal anisotropy of intermediate-period surface waves (abstract), *EOS, Trans. Am. geophys. Un.,* **82**(47), S51E–06.

Ekström, G. & Dziewonski, A.M., 1998. The unique anisotropy of the Pacific upper mantle, *Nature,* **394,** 168–172.

Fornberg, B., 1996. *A Practical Guide to Pseudospectral Methods,* Cambridge University Press, Cambridge.

Forsyth, D.W., 1975. The early structural evolution and anisotropy of the oceanic upper mantle, *Geophys. J. R. astr. Soc.,* **43,** 103–162.

Fouch, M.J. & Fischer, K.M., 1998. Shear wave anisotropy in the Mariana subduction zone, *Geophys. Res. Lett.,* **25,** 1221–1224.

Gaboret, C., Forte, A.M. & Montagner, J.-P., 2003. The unique dynamics of the Pacific Hemisphere mantle and its signature on seismic anisotropy, *Earth planet. Sci. Lett.,* **208,** 219–233.

Gordon, R.G. & Jurdy, D.M., 1986. Cenozoic global plate motions, *J. geophys. Res.,* **91,** 12 389–12 406.

Gudmundsson, O. & Sambridge, M., 1998. A regionalized upper mantle (RUM) seismic model, *J. geophys. Res.,* **103,** 7121–7136.

Hager, B.H. & Clayton, R.W., 1989. Constraints on the structure of mantle convection using seismic observations, flow models, and the geoid, in *Mantle Convection; Plate Tectonics and Global Dynamics, The Fluid Mechanics of Astrophysics and Geophysics,* Vol. 4, pp. 657–763, ed. Peltier, W.R., Gordon and Breach, New York.

Hager, B.H. & O'Connell, R.J., 1981. A simple global model of plate dynamics and mantle convection, *J. geophys. Res.,* **86,** 4843–4867.

Hall, C.E., Fischer, K.M. & Parmentier, E.M., 2000. The influence of plate motions on three-dimensional back arc mantle flow and shear wave splitting, *J. geophys. Res.,* **105,** 28 009–28 033.

Hess, H.H., 1964. Seismic anisotropy of the uppermost mantle under oceans, *Nature,* **203,** 629–631.

Ji, S., Zhao, X. & Francis, D., 1994. Calibration of shear-wave splitting in the subcontinental upper mantle beneath active orogenic belts using ultramafic xenoliths from the Canadian Cordillera and Alaska, *Tectonophysics,* **239,** 1–27.

Jung, H. & Karato, S.-i., 2001. Water-induced fabric transitions in olivine, *Science,* **293,** 1460–1463.

Kaminski, É. & Ribe, N.M., 2001. A kinematic model for for recrystallization and texture development in olivine polycrystals, *Earth planet. Sci. Lett.,* **189,** 253–267.

Kaminski, É. & Ribe, N.M., 2002. Time scales for the evolution of seismic anisotropy in mantle flow, *Geochem. Geophys. Geosyst.,* **3** (2001GC000222).

Karato, S.-i., 1998. Seismic anisotropy in the deep mantle, boundary layers and the geometry of convection, *Pure appl. Geophys.,* **151,** 565–587.

Laske, G. & Masters, G., 1998. Surface-wave polarization data and global anisotropic structure, *Geophys. J. Int.,* **132,** 508–520.

Lithgow-Bertelloni, C. & Richards, M.A., 1998. The dynamics of Cenozoic and Mesozoic plate motions, *Rev. Geophys.,* **36,** 27–78.

Lithgow-Bertelloni, C. & Silver, P.G., 1998. Dynamic topography, plate driving forces and the African superswell, *Nature,* **395,** 269–272.

Lithgow-Bertelloni, C., Richards, M.A., Ricard, Y., O'Connell, R.J. & Engebretson, D.C., 1993. Toroidal–poloidal partitioning of plate motions since 120 Ma, *Geophys. Res. Lett.,* **20,** 375–378.

Little, T.A., Savage, M.K. & Tikoff, B., 2002. Relationship between crustal finite strain and seismic anisotropy in the mantle, Pacific–Australia plate boundary zone, South Island, New Zealand, *Geophys. J. Int.,* **151,** 106–116.

Love, A.E.H., 1927. *A Treatise on the Mathematical Theory of Elasticity,* Cambridge University Press, Cambridge (reprinted in 1944 by Dover, New York).

Mainprice, D., Barruol, G. & Ben Ismail, W., 2000. The seimic anisotropy of the Earth's mantle: from single crystal to polycrystal, in *Earth's Deep Interior. Mineral Physics and Tomography from the Atomic to the Global Scale,* Vol. 117, pp. 237–264, eds Karato, S.-i., Forte, A.M., Liebermann, R.C., Masters, G. & Stixrude, L., Geophysical Monograph, American Geophysical Union, Washington, DC.

McKenzie, D.P., 1979. Finite deformation during fluid flow, *Geophys. J. R. astr. Soc.,* **58,** 689–715.

McKenzie, D. & Jackson, J., 1983. The relationship between strain rates, crustal thickening, paleomagnetism, finite strain and fault movements within a deforming zone, *Earth planet. Sci. Lett.,* **65,** 182–202.

Mitrovica, J.X. & Forte, A.M., 1997. Radial profile of mantle viscosity: results from the joint inversion of convection and postglacial rebound observables, *J. geophys. Res.,* **102,** 2751–2769.

Montagner, J.-P., 1994. What can seismology tell us about mantle convection?, *Rev. Geophys.,* **32,** 115–137.

Montagner, J.-P., 1998. Where can seismic anisotropy be detected in the Earth's mantle? In boundary layers, *Pure appl. Geophys.,* **151,** 223–256.

Montagner, J.-P., 2002. Upper mantle low anisotropy channels below the Pacific Plate, *Earth planet. Sci. Lett.,* **202,** 263–274.

Montagner, J.-P. & Guillot, L., 2000. Seismic anisotropy in the Earth's mantle, in *Problems in Geophysics for the New Millenium,* pp. 217–253, eds Boschi, E., Ekström, G. & Morelli, A., Istituto Nazionale di Geofisica e Vulcanologia, Editrice Compositori, Bologna.

Montagner, J.-P. & Nataf, H.-C., 1986. A simple method for inverting the azimuthal anisotropy of surface waves, *J. geophys. Res.,* **91,** 511–520.

Montagner, J.-P. & Tanimoto, T., 1991. Global upper mantle tomography of seismic velocities and anisotropies, *J. geophys. Res.,* **96,** 20 337–20 351.

Montagner, J.-P., Griot-Pommera, D.-A. & Laveé, J., 2000. How to relate body wave and surface wave anisotropy?, *J. geophys. Res.,* **105,** 19 015–19 027.

Mooney, W.D., Laske, G. & Masters, G., 1998. CRUST 5.1: a global crustal model at 5 degrees × 5 degrees, *J. geophys. Res.,* **103,** 727–747.

Nataf, H.-C. & Ricard, Y., 1996. 3SMAC: an *a priori* tomographic model of the upper mantle based on geophysical modeling, *Phys. Earth planet. Inter.,* **95,** 101–122.

Nicolas, A. & Christensen, N.I., 1987. Formation of anisotropy in upper mantle peridotites; a review, in *Composition, Structure and Dynamics of the Lithosphere–Asthenosphere System,* Vol. 16, *Geodynamics,* pp. 111–123, eds Fuchs, K. & Froidevaux, C., American Geophysical Union, Washington, DC.

Nishimura, C.E. & Forsyth, D.W., 1989. The anisotropic structure of the upper mantle in the Pacific, *Geophys. J.,* **96,** 203–229.

O'Connell, R.J., Gable, C.W. & Hager, B.H., 1991. Toroidal–poloidal partitioning of lithospheric plate motions, in *Glacial Isostasy, Sea-Level and Mantle Rheology,* pp. 535–551, ed. Sabadini, R., Kluwer, Amsterdam.

Panasyuk, S.V. & Hager, B.H., 1998. A model of transformational superplasticity of the upper mantle, *Geophys. J. Int.,* **133,** 741–755.

Peselnick, L. & Nicolas, A., 1978. Seismic anisotropy in an ophiolite peridotite. Application to oceanic upper mantle, *Geophys. Res. Lett.,* **83,** 1227–1235.

Polet, J. & Kanamori, H., 2002. Anisotropy beneath California: shear wave splitting measurements using a dense broadband array, *Geophys. J. Int.,* **149,** 31–327.

Press, W.H., Teukolsky, S.A., Vetterling, W.T. & Flannery, B.P., 1993. *Numerical Recipes in C: the Art of Scientific Computing,* 2nd edn, Cambridge University Press, Cambridge.

Ranalli, G., 1995. *Rheology of the Earth,* 2nd edn, Chapman & Hall, London.

Ribe, N.M., 1989. Seismic anisotropy and mantle flow, *J. geophys. Res.,* **94,** 4213–4223.

Ribe, N.M., 1992. On the relation between seismic anisotropy and finite strain, *J. geophys. Res.,* **97,** 8737–8747.

Ricard, Y. & Vigny, C., 1989. Mantle dynamics with induced plate tectonics, *J. geophys. Res.,* **94,** 17 543–17 559.

Ricard, Y., Doglioni, C. & Sabadini, R., 1991. Differential rotation between lithosphere and mantle: a consequence of lateral mantle viscosity variations, *J. geophys. Res.,* **96,** 8407–8415.

Romanowicz, B. & Snieder, R., 1988. A new formalism for the effect of lateral heterogeneity on normal modes and surface waves. II. General anisotropic perturbation, *Geophys. J.,* **93,** 91–99.

Russo, R.M. & Silver, P.G., 1994. Trench-parallel flow beneath the Nazca plate from seismic anisotropy, *Science,* **263,** 1105–1111.

Saltzer, R.L., Gaherty, J.B. & Jordan, T.H., 2000. How are vertical shear wave splitting measurements affected by variations in the orientation of azimuthal anisotropy with depth?, *Geophys. J. Int.,* **141,** 374–390.

Savage, M.K., 1999. Seismic anisotropy and mantle deformation: What have we learned from shear wave splitting?, *Rev. Geophys.,* **37,** 65–106.

Schott, B., Yuen, D.A. & Schmeling, H., 2000. The significance of shear heating in continental delamination, *Phys. Earth planet. Inter.,* **118,** 273–290.

Schulte-Pelkum, V. & Blackman, D.K., 2003. A synthesis of seismic *P* and *S* anisotropy, *Geophys. J. Int.,* **154,** 166–178.

Schulte-Pelkum, V., Masters, G. & Shearer, P.M., 2001. Upper mantle anistropy from long-period *P* polarization, *J. geophys. Res.,* **106,** 21 917–21 934.

Silver, P.G., 1996. Seismic anisotropy beneath the continents: probing the depths of geology, *Ann. Rev. Earth Planet. Sci.,* **24,** 385–432.

Simons, F.J. & van der Hilst, R.D., 2003. Seismic and mechanical anisotropy and the past and present deformation of the Australian lithosphere, *Earth planet. Sci. Lett.,* **211,** 271–286.

Smith, M.L. & Dahlen, F.A., 1973. The azimuthal dependence of Love and Rayleigh wave propagation in a slightly anisotropic medium, *J. geophys. Res.,* **78,** 3321–3333.

Steinberger, B., 2000. Slabs in the lower mantle—results of dynamic modelling compared with tomographic images and the geoid, *Phys. Earth planet. Inter.,* **118,** 241–257.

Steinberger, B. & O'Connell, R.J., 1998. Advection of plumes in mantle flow: implications for hotspot motion, mantle viscosity, and plume distribution, *Geophys. J. Int.,* **132,** 412–434.

Steinberger, B., Schmeling, H. & Marquart, G., 2001. Large-scale lithospheric stress field and topography induced by global mantle circulation, *Earth planet. Sci. Lett.,* **186,** 75–91.

Tanimoto, T. & Anderson, D.L., 1985. Lateral heterogeneity and azimuthal anisotropy of the upper mantle: Love and Rayleigh waves 100–250 s, *J. geophys. Res.,* **90,** 1842–1858.

Tommasi, A., 1998. Forward modeling of the development of seismic anisotropy in the upper mantle, *Earth planet. Sci. Lett.,* **160,** 1–13.

Tommasi, A., Mainprice, D., Canova, G. & Chastel, Y., 2000. Viscoplastic self-consistent and equilibrium-based modelling of olivine lattice preferred orientation. 1. Implications for the upper mantle seismic anisotropy, *J. geophys. Res.,* **105,** 7893–7908.

van Keken, P. & Zhong, S., 1999. Mixing in a 3D spherical model of present-day mantle convection, *Earth planet. Sci. Lett.,* **171,** 533–547.

Vinnik, L.P., Farra, V. & Romanowicz, B., 1989. Azimuthal anisotropy in the Earth from observations of *SKS* at Geoscope and Nars broadband stations, *Bull. seism. Soc. Am.,* **79,** 1542–1558.

Vinnik, L.P., Makeyeva, L.I., Milev, A. & Usenko, Y., 1992. Global patterns of azimuthal anisotropy and deformation in the continental mantle, *Geophys. J. Int.,* **111,** 433–447.

Wenk, H.-R. & Tomé, C.N., 1999. Modeling dynamic recrystallization of olivine aggregates deformed in simple shear, *J. geophys. Res.,* **104,** 25 513–25 527.

Wenk, H.-R., Bennett, K., Canova, G.R. & Molinari, A., 1991. Modelling plastic deformation of peridotite with the self-consistent theory, *J. geophys. Res.,* **96,** 8337–8349.

Wessel, P. & Smith, W.H.F., 1991. Free software helps map and display data, *EOS, Trans. Am. geophys. Un.,* **72,** 445–446.

Wolfe, C.J. & Solomon, S.C., 1998. Shear-wave splitting and implications for mantle flow beneath the MELT region of the East Pacific rise, *Science,* **280,** 1230–1232.

Zhang, S. & Karato, S.-i., 1995. Lattice preferred orientation of olivine aggregates deformed in simple shear, *Nature,* **375,** 774–777.

APPENDIX: DEPTH SENSITIVITY OF SURFACE WAVES TO AZIMUTHAL ANISOTROPY

Our treatment closely follows that of Montagner & Nataf (1986) and Montagner & Tanimoto (1991). The eigenfunctions of high-ℓ normal modes can be used to construct Fréchet derivatives (or *sensitivity kernels*), K_m, that characterize the effect of small perturbations in a parameter m at a certain depth r on changing the phase velocity c of a surface wave:

$$k_m(c, r) = mK_m = m\frac{\partial c}{\partial m}. \tag{A1}$$

Here, m stands for an elastic modulus or density ρ (e.g. Dahlen & Tromp 1998, p. 335ff). For a transversely isotropic Earth model such as PREM, the elasticity tensor is reduced from its most general form with 21 independent components to five constants, A, C, F, L and N in the notation of Love (1927). We write the perturbations in c in a transversely isotropic medium as

$$dc \approx \int_0^R \left(\frac{dC}{C}k_C + \frac{dA}{A}k_A + \frac{dL}{L}k_L + \frac{dN}{N}k_N + \frac{dF}{F}k_F + \frac{d\rho}{\rho}k_\rho \right). \tag{A2}$$

For wave propagation in an elastic medium that has the most general form of anisotropy, Smith & Dahlen (1973) showed that the azimuthal dependence of Love and Rayleigh wave speed anomalies can be expanded as given in eq. (1). Montagner & Nataf (1986) demonstrated that the sensitivity kernels for the D terms can be retrieved from the kernels already constructed for transversely isotropic models as in eq. (A2). Montagner & Nataf also found that the 4ϕ terms

Table A1. Ratios of elastic coefficients for 2ϕ contributions as in eq. (A3) for two different rock samples from the indicated sources. cos and sin denote the C, S constants. Since the partitioning of these ratios depends on the horizontal coordinate frame, we also give the amplitude $\sqrt{\cos^2 + \sin^2}_{\rm norm}$, normalized by the maximum ratio in each row.

Type	$\frac{B_{C,S}}{A}$	$\frac{H_{C,S}}{F}$	$\frac{G_{C,S}}{L}$
	Peselnick & Nicolas (1978)		
cos	0.034	0.003	0.028
sin	−0.002	0.006	−0.008
$\sqrt{\cos^2 + \sin^2}_{\rm norm}$	1.0	0.176	0.853
	Nunuvak (Ji *et al*. 1994)		
cos	0.075	0.014	0.054
sin	−0.009	−0.004	−0.009
$\sqrt{\cos^2 + \sin^2}_{\rm norm}$	1.0	0.197	0.724

should generally be small for predominantly horizontal alignment of fast propagation axes based on measurements of elasticity tensors from the field. Rayleigh waves are more sensitive to the 2ϕ component than Love waves, and only the 2ϕ term is readily interpreted in terms of fast horizontal propagation axes in a strained medium with lattice-preferred orientation. Following our expectations, the observed 4ϕ signal is smaller than the 2ϕ signal in most regions, with aforementioned exception in regions of radial flow (Section 2).

We shall therefore focus on $D^{2\phi}$ for Rayleigh waves. Montagner & Nataf (1986) find that sensitivity kernels for the cos(2ϕ) and sin(2ϕ) terms can be written as

$$k^{\rm Rayleigh}_{\cos(2\phi),\sin(2\phi)} = \frac{B_{C,S}}{A} k_A + \frac{H_{C,S}}{F} k_F + \frac{G_{C,S}}{L} k_L. \qquad \text{(A3)}$$

The six fractions with $B_{C,S}$, $H_{C,S}$ and $G_{C,S}$ are simple functions of C_{ij} (Montagner & Nataf 1986, eq. 5) and determine the relative weights of the $k_{A,F,L}$ kernels. While Montagner & Nataf's (1986) analysis of the effect of anisotropy was restricted to a flat Earth, Romanowicz & Snieder (1988) were able to recover Montagner & Nataf's approximation asymptotically for large ℓ in a more complete treatment. Following Montagner & Tanimoto (1991), we can therefore obtain the depth sensitivity of Rayleigh waves to azimuthal anisotropy with eq. (A3) if we use elastic moduli for some representative anisotropic material whose fast propagation axis is assumed to be in the horizontal plane. Table A1 lists the relevant parameters for an oceanic sample from Peselnick & Nicolas (1978) (as used by Montagner & Nataf 1986) and for Nunuvak from Ji *et al.*'s (1994) data (as used by Savage 1999). The $B_{C,S}$ and $G_{C,S}$ ratios are consistently larger than the $H_{C,S}$ ratio. Since the k_L kernel is additionally somewhat larger than k_A and k_F, the $G_{C,S}/Lk_L$ term is mostly responsible for the depth sensitivity of Rayleigh waves to the 2ϕ anisotropy, shown in Fig. A1 for surface waves with periods of $T = 50$, 100 and 150 s.

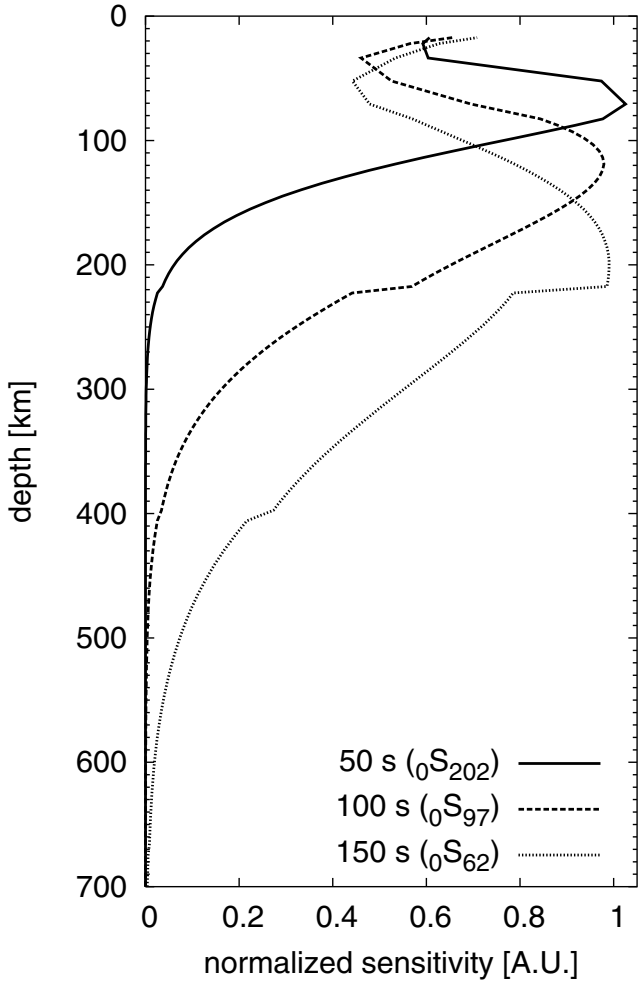

Figure A1. $D^{2\phi}$ sensitivity kernels for Rayleigh waves with periods of 50, 100 and 150 s for anisotropic PREM, normalized to their respective maximum value. Kernels are shown for the amplitude of all 2ϕ terms and are calculated from eq. (A3) and the data of Peselnick & Nicolas (1978) in Table A1.

Phase-velocity sensitivity kernels were estimated based on normal-mode eigenfunctions computed for radially anisotropic PREM with the MINEOS program by G. Masters (e.g. Dahlen & Tromp 1998, p. 335). For the elastic parameters under consideration, the sensitivity of Rayleigh waves to azimuthal anisotropy has a depth dependence that is very similar to their $k_{V_{SV}}$ kernels. We use the 2ϕ kernels to average the horizontal projections of the inferred fast-propagation axes from strain at each depth when we compare our modelling results with surface-wave-based anisotropy.